Modern travertine precipitation at Lýsuhóll hot springs, Snæfellnes, Iceland: implications for calcite crystal growth

Brian Jones[1], Robin W. Renaut[2]

[1] *Brian Jones, Department of Earth and Atmospheric Sciences, University of Alberta, Edmonton, Alberta, T6G 2E3, Canada (E-mail: Brian.Jones@ualberta.ca)*

[2] *Robin W. Renaut, Department of Geological Sciences, University of Saskatchewan, Saskatoon, Saskatchewan, S7N 5E2, Canada (E-mail: robin.renaut@usask.ca)*

Abstract:

Three thermal springs, at Lýsuhóll on Snæfellnes Peninsula on the west coast of Iceland, with vent water temperatures of 20 to 46°C are characterized by thriving microbial mats that mediate the precipitation of opal-A, Fe-rich opal-A, Fe-rich reticulate coatings, and calcite that are intermixed with each other at micro- to macro-scales. Although many of the microbes are preserved by silicification, there is no evidence of preservation by calcification. The calcite crystals that grew in the confines of the microbial mats, despite not being perfectly formed and < 1 mm long, can be divided into prismatic forms (types I to III), trigonal prisms, dodecahedrons, plates, rhombic forms (types I to III), and dendrites. Apart from the dendrites, all of the other crystals are mesocrystals formed of nanocrystals that are aligned in perfect crystallographic registers. All of these crystals grew through the non-classical crystal growth model, which is a particle-based system. In this case, the growth of the nanocrystals and the development of the mesocrystals took place in the microdomains that developed in the biofilms. Recognition of this type of crystal growth in older spring deposits may be difficult because (1) the mesocrystals may be transformed to monocrystals by fusion of the nanocrystals, (2) evidence of the microbes and biofilm may be missing because they are commonly lost to decay before preservation by calcification can take place, and/or (3) these mesocrystals may become the main nucleation centers for larger calcite crystals that grow via the classical crystal growth model. Irrespective of these nuances, the possibility that calcite crystals initially developed as mesocrystals should be a critical consideration in the evaluation of any spring system where calcite is being precipitated.

Keywords: Thermal springs, calcite, mesocrystals, biofilms, silicification, calcification

INTRODUCTION

In spring systems, the precipitation of calcite and crystal morphogenesis have been attributed to many parameters, including water temperature (T), the Mg:Ca ratio of the spring water, the CO_2 content of the fluid and rate of degassing, and/or the presence of microbial mats (Chafetz and Folk 1984; Folk 1994; Pentecost 2005; Jones 2017a). In many springs, the resident microbiota and the biofilms that they generate can have a significant impact on mineral precipitation with microscale variations in the types of precipitate and crystal morphologies being readily apparent (e.g., Jones and Peng 2014b, 2016b). In spring systems where biofilms mediate crystal growth it is becoming increasingly apparent that the precipitation and crystal morphogenesis is highly variable at the microscale and commonly develops via non-classical growth mechanisms (e.g., Jones and Peng 2012, 2014b, 2016b; Jones 2017a). This premise is further investigated in this study by examining the factors that controlled growth of many different types of calcite crystals in the spring environs found at Lýsuhóll, which is located on the south side of Snæfellnes Peninsula on the west coast of Iceland (Fig. 1).

The presence of calcite deposits at Lýsuhóll has been debated ever since Kjartansson (1947) first made note of travertine in the area. Later, Tulinius et al. (1991), Friðleifsson (1992), and Friðleifsson and Ármannsson (1999) argued that those spring deposits are formed largely of siliceous sinter and that only minor amounts of travertine are present. Tazaki et al. (1995) described calcite associated with microbial mats from hot springs at Lýsuhóll. Jones et al. (2005) clearly demonstrated that travertines are present at Lýsuhóll, when they described the calcite precipitates, formed of complex calcite dendrites, that had formed around a spring that is now inactive. Other studies of the spring deposits at Lýsuhóll appear to have focused largely on Stjáni, which is an active spring located beside Hrútsgill (Fig. 1B). Unfortunately, many of these studies did not provide exact locations of their sample sites and it is not always clear if the samples were collected from Stjáni or from some of the smaller springs that are found in the horse paddock on the opposite side of the road to the west of Stjáni. In most cases, these studies have focused on the mineralization that is associated with the microbes found on the discharge apron (Tazaki 1995; Konhauser and Ferris 1996; Tazaki 1999). Owen et al. (2008) examined modern diatoms from Lýsuhóll as part of their overall assessment of diatoms found in geothermal systems worldwide. Pentecost (2011) provided an assessment of the microbes found on the discharge apron in the Stjáni system.

This study focuses on the calcite deposits associated with Stjáni spring, which is located beside Hrútsgill (Figs. 1, 2A, 3), and springs LY-2 and LY-3, which are located on the west side of the horse paddock that lies to the west of Stjáni (Figs. 1, 2B, C, 3, 4). Based on systematic sampling of the precipitates and high-resolution, high-magnification scanning electron images of numerous samples, this paper (1) describes the different types of calcite crystals that have developed in the microbial mats of these spring systems, (2) describes the spatial and temporal association of the calcite with the opal-A, Fe-rich opal-A, and Fe-rich reticulate coatings, and (3) examines the relationships between the spring water chemistry, the microbial mats, and the precipitates found on the discharge aprons. Integration of this information shows that much of the calcite precipitation took place within the microbial mats with non-classical crystal growth mechanism being the norm.

GEOLOGICAL SETTING

Hot and cold springs on Snæfellnes Peninsula are characterized by high CO_2 emissions, including free CO_2 gas that probably comes from deep-seated intrusions and/or the mantle (Arnórsson and Barnes 1983). Lýsuhóll, located on the southern coastal plain of Snæfellnes

Peninsula in western Iceland (Fig. 1), experiences a mean annual temperature of ~ 4°C and ~ 1200 mm/year precipitation. The springs are located ~ 2.5 km north of the Atlantic shoreline at the base of an escarpment that is 700 m high and formed of late Neogene to Holocene volcanic rocks (Sigurdsson 1970b; Sigurdsson 1970a; Einarsson 1994; Jóhannesson and Sæmundsson 1998).

Fossil hot-spring deposits, formed of siliceous sinter and calcite, cover an area of ~ 250 x 350 m west of Hrútsgill on private farmland that is now used as a horse paddock (Fig. 2A). Travertine deposits, found in the northern part of the site, are younger than the siliceous sinters on which they rest, recording the change from a higher-temperature to lower-temperature geothermal system (Jones et al. 2005; Thomas et al. 2016). Today, surface runoff is restricted largely to narrow, shallow streams that drain water from the surrounding area and shallow pools in some of the lower lying areas (Fig. 2A). The north-central part of the spring site is covered by numerous loose and broken blocks of spring deposits with little material being *in situ*. Although formed largely of siliceous sinter, scattered blocks of hard dense calcite are also present.

In August 2005, three active springs, herein numbered LY1 (Stjáni), LY2, and LY3, were found in this area (Figs. 2, 3). Stjáni (Fig. 3) is located beside Hrútsgill, whereas LY-2 (Fig. 2B) and LY-3 (Fig. 2C) are located on the west side of the horse paddock (Fig. 2A).

Stjáni

Stjáni, which is the largest active spring today, is located close to Hrútsgill (Fig. 2A, 3). This is the spring that Pentecost (2011) referred to as Stjáni and it is probably the same spring that is listed by White et al. (1963, their Tables 25, 28) and Waring (1965, p. 103). This may be the spring from which Tazaki et al. (1995) and Tazaki (1999) described crystalline calcite and non-crystalline silica that was found with the various types of microbial mats.

The spring water, with a temperature (T) of 57°C and pH of 6.7 (August 2005), discharges from a pipe that feeds water into a pool that is surrounded by a concrete retaining wall (Fig. 3B). A break in the pipe has led to development of another pool that surrounds the concrete pool (Fig. 3B). The discharge apron, developed on the west side of these pools, is ~ 23 m long and 13 m wide (Fig. 3A). Water T decreases to ~ 15°C on the distal parts of the main discharge apron. In July 2004, well-developed microbial mats covered the discharge apron and the underlying precipitates were barely visible (Fig. 3C, D). In late August 2005, the discharge apron had a different appearance with microbial mats being restricted to the proximal part of the discharge apron (Fig. 3B) and calcite precipitates being visible on the distal part of the apron (Fig. 3E). The microbial mats are either attached to the substrate or float on the surfaces of the pools.

The discharge apron surface is covered by calcite precipitated from spring water. The proximal part, which is relatively flat, is characterized by small pools floored by well-developed microbial mats. Rimstone pools, typically < 1 cm deep and bounded by rimstone dams, characterize the middle and distal parts of the discharge apron (Fig. 3E). Pieces of grass and the stems of rooted grass that are below water level are commonly encrusted by calcite.

On the south side of the site, a building houses a pump that extracts hot water for use in the local houses. Access to that building is across the upper part of the discharge apron. Thus, in August 2005, tire tracks that cut across the upper part of the discharge apron were diverting outflowing spring waters laterally and away from the main discharge apron. In some of the pools, biofilms coat the substrate and formed floating microbial mats are commonly centered around actively growing grass (Fig. 3F). Bushes of dendrite calcite crystals, up to 3 cm high and commonly nucleated around grass stems, were found in the deeper parts of the tire ruts (Fig. 3G).

Springs LY-2 and LY-3

Both springs, which have vents < 20 cm in diameter, discharge water that flows into one of the small streams that flows across the horse paddock (Figs. 2B, C, 4A, E). When measured, water with a T of 20.3°C and pH of 6.3 was ejected from spring LY-2, whereas water with a T of 37.3°C and pH of 6.2 issued from spring LY-3. Distally widening, triangular-shaped discharge aprons characterize both springs (Fig. 2B, C). The apron at LY-2 is up to 4.5 m long and 4.0 m wide, whereas the apron at LY-3 is 9 m long and 10 m wide.

At each spring, the water ejected from the vent is funneled through narrow (< 0.5 m wide) channels that are coated with red ferrihydrite surface coatings (Fig. 4A, B, E). Just downstream from the vents, green microbial streamers, up to 25 cm long, are attached to subaqueous channel margins (Fig. 4A, B). The middle and distal parts of the discharge aprons are characterized by (1) very shallow (< 3 cm) sheetflow and the spring water cools rapidly downslope; (2) yellowish-red calcite precipitates; and (3) well-developed biofilms (Fig. 4). Shallow rimstone pools are the main architectural features of the middle and distal parts of the discharge aprons at LY-2 and LY-3 (Fig. 4C, F). Fine-grained sediment commonly covers the floors of these shallow pools (Fig. 4C, D, F, G) and small (< 5 mm long), thin-shelled gastropods are present in many of them (Fig. 4G). Some of the carbonate detritus in these pools may be fecal pellets produced by the gastropods. Locally, on the distal parts of the discharge aprons of LY-2 and LY-3, there are numerous small, mucus rich-mounds that are up to 5 mm high (Fig. 4H). These soft masses, which have a slightly greenish hue, contain numerous small crystalline calcite rosettes. Biofilms cover most of the discharge aprons.

SAMPLES AND METHODS

Samples from springs Stjáni, LY-2, and LY-3 were collected with a permit from Umhverfissofuun Háskóla Íslands and permission of the land owners.

The discharge apron below Stjáni is formed of calcite with minor intercalations of siliceous sinter whereas the discharge aprons at springs LY-2 and LY-3 are covered with siliceous sinter, Fe-rich precipitates, and calcite. For each spring, sampling followed a systematic proximal to distal pattern (Figs. 2B, 2C, 3A). Surface samples were the main focus because of the need to examine recently formed precipitates that had undergone minimal diagenetic change. The mucus- and microbial-rich samples were placed in sealed containers in order to minimize the changes that might occur between the time of collection and the time of examination on the SEM. Sampling was kept at a minimum in order to avoid excessive damage to the sites, particularly at Stjáni.

Water T and pH were measured in the field with water T being confirmed through the use of three different thermometers. Water samples collected in August, 2005 came from Stjáni; LY-2 and LY-3 that came from the vents of springs LY-2 and LY-3 (Fig. 1); LY-4 that came from a small stream on the north side of the fence, close to LY-2 and LY-3; and LY-5 came from a small pond downstream from the outflows from LY-2 and LY-3 (Fig. 1). For each site, the samples included (1) 100 ml of filtered water collected using a syringe with a 0.22 μm pore filter, and (2) 200 ml of unfiltered water. Water samples were analyzed by the Saskatchewan Research Council, Canada, within one month of collection, by atomic absorption spectrometry (Na, K, Ca, Mg, Si), ion chromatography (SO_4), ion specific electrodes (Cl, F, Li), and titration (HCO_3, CO_3).

The bulk mineralogy of each sample was confirmed by X-ray diffraction (XRD) analysis. Such analyses used samples, each weighing ~ 1 g, that were ground to a fine powder using a mortar and pestle. The samples were analyzed on a Rigaku Geigerflex sealed X-ray generator with a Co tube and current of 40 kV and 35 mA. Mineral identifications are based on the scan results using the JADE subroutine that is linked to the XRD instrument.

Small fractured pieces of each sample were mounted on stubs and sputter coated with a thin layer of gold before being examined on a JEOL 6301FE field emission scanning electron microscope (SEM) at an accelerating voltage of 5 kV. Energy dispersive analysis (EDX) analysis on the SEM, with an accelerating voltage of 20kV, was used to determine the elemental composition of specific parts of the samples. Given that the different mineral phases are integrated at the microscale, it was impossible to segregate each phase for X-ray Diffraction (XRD) analysis. In many samples, the amount of some precipitates was too low (probably < 2%) to show on XRD of bulk samples. Thus, identification of each precipitate was based on its morphology and elemental content as determined by EDX. For each precipitate, numerous EDX analyses were undertaken in order to ensure that the detected elements did not come from the background.

This paper is based largely on the 1584 SEM photomicrographs that were obtained from these samples. Adobe Photoshop CC2017© was used to adjust the brightness and contrast of the digital field and SEM images used in this paper.

TERMINOLOGY

The terminology used for the calcite crystals found in the samples from Lýsuhóll follows that proposed by Jones (2017a). Thus, a mesocrystal, which is an abbreviation for a “mesoscopically structured crystal”, is defined as a colloidal crystal that is formed of nanocrystals that are "…aligned in common crystallographic register…. such that the mesocrystal scatters X-rays or electrons like a single crystal and shows birefringence properties of a single crystal" (Meldrum and Cölfen 2008, p. 4343). This term includes "composite crystals" as described by Given and Wilkinson (1985), Sandberg (1985) Jones and Renaut (1996b), "aggregate crystals" as described by Brinkley et al. (1980), Chafetz et al. (1985), and Jones (1989), and polycrystalline crystals as described by Towe (1967). The nanocrystals that form the mesocrystals are equivalent to crystallites or subcrystals as described by Sandberg (1985), Jones (1989), and Jones and Renaut (1996b).

RESULTS

The discharge aprons below the spring vents at Stjáni, LY-2, and LY-3 are formed of intercalated opal-A, Fe-rich opal-A, Fe-rich precipitates, and calcite (Fig. 5). At LY-2 and LY-3, the precipitates, which are vivid red reflecting their high Fe content, are found in and around the spring vents (Fig. 4A, B, E). In general, opal-A is more common in the proximal areas, whereas calcite is more common in the distal areas. The light to dark orange color of the calcite reflects the presence of Fe. The poorly defined laminations evident in some of the samples reflect (1) variations in the microbiota with mats formed of filamentous microbes commonly alternating with layers that are largely devoid of microbes (Fig. 5A), (2) alternation between layers formed of opal-A and Fe-rich opal A (Fig. 5A), or (3) alternations between laminae formed of opal-A or Fe-rich opal-A and calcite (Fig. 5B, C). Preserved microbes are locally common in the opal-A laminae but rare in the calcite laminae.

Water chemistry

When sampled, waters at the vents of the three springs examined in this study had temperatures of 20 to 46.1°C, pH of 6.2 to 6.6, high Na (373–434 mg l^{-1}) and HCO_3 (1100–1350 mg l^{-1}) concentrations with the Ca content (37–62 mg l^{-1}) being significantly higher than Mg (16 to 26 mg l^{-1}) (Table 1). These spring waters also have high SiO_2 (up to 219 mg l^{-1}) and Fe (0.22 to 0.53 mg l^{-1}).

Pentecost (2011) suggested that the water analysis reported by White et al. (1963, their Table 25) came from Stjáni although they did not list it under that name. Similarly, we assume that other analyses in Arnórsson and Barnes (1983), Fridleifsson and Ármannsson, (1999) Kjartansdóttir (2014) come from Stjáni because they have similar compositions in Na, Cl, B, SiO_2 and pH to LY1. Alkaline earths (Ca, Mg) and Fe are more variable. It is unclear if these differences reflect temporal changes in water composition or the site of sampling. The higher pH, and different salinities, solute concentrations, and Na/Cl ratios in the distal lower-temperature waters (LY-4 and 5) probably reflect local mixing of fluids (spring outflow and runoff) and exsolution of CO_2.

Table 1 shows the saturation indices with respect to calcite and amorphous silica for samples LS1 to 5, calculated using SOLMINEQ88 (Kharaka et al. 1988). The results imply that calcite is close to equilibrium at the spring vents and saturated in the ponded water downstream. Silica saturation levels are similar to those of calcite at the vents and marginally higher at LY-2 and 3, but silica is undersaturated in stream water and the distal pond. These few samples are insufficient to draw conclusions, but they imply that minor changes in physicochemical conditions, with or without biological influences, might be enough for calcite and opal-A to precipitate near the vents.

Many springs on Snæfellnes Peninsula have high CO_2 emissions (e.g., Barth 1950, his Table 15; White et al. 1963, their Table 28; Thomas et al. 2016), with CO_2 forming up 93% of the non-condensable gases.

Microbes and biofilms

Extant microbial consortia. – Tazaki et al. (1995) showed that the microbial mats at one Lýsuhóll spring contain many taxa, including the cyanobacteria (cyanoprokaryotes) *Anabaena, Oscillatoria, Fischerella, Cylindrospermum, Synechocystis,* and *Synechococcus*. Although the location of that spring is unclear, their description of the site implies that it was Stjáni.

Pentecost (2011, his Table 2), based on samples collected from around the main pool at Stjáni, suggested that the microbial mats were then formed of cyanobacteria (*Aphanocapsa endolithica* Ercegovic*, A. microscopica* Naegeli*, Calothrix thermalis* (Schwabe) Hansgirg*, Oscillatoria formosa* Bory*, Pleurocapsa minor* Hansgirg emend. Geitler, *Mastigocladus laminosus* f. *phormidiodes* Boye-Petersen*, Phormidium ambiguum* Gomont, *P. laminosum* Gomont, *Scytonema* sp., and *Synechocystis crassa* Woronichan); Bacillariophyta (*Amphora pediculus* (Kuetzing) Grunow, *Fragilaria construens* f. *venter* (Ehrenberg) Hustedt), and Rhodophyta (*Chroothece mobilis* Pasher et Petrova). The most common forms were *Calothrix thermalis and Phormidium ambiguum,* whereas the other named species were present locally in small numbers.

At Stjáni, LY-2, and LY-3, benthic samples from substrates and pools show that (1) the biofilms are formed of complex arrays of intertwined filaments and copious amounts of extracellular polymeric substances (EPS) (Fig. 6); (2) isolated calcite crystals or clusters of crystals are scattered throughout the biofilm (Fig. 6A–B); and (3) opal-A spheres are common on surfaces of the EPS and are locally concentrated around filamentous microbes that form the framework of the biofilm (Fig. 6C, D). In some examples, the biofilms cover calcite crystals that are attached to the substrate, whereas in other examples, the calcite crystals are unattached and float in the biofilm (Fig. 6A, B).

Mineralized microbes.– Microbes preserved in opal-A and Fe-rich opal-A are common (Fig. 7), whereas calcified microbes are very rare. Silicification, which involved replacement of the microbes by opal-A, produced well-preserved microbes with many of their morphological features being intact. The most common silicified filamentous microbes belong to the form-genus *Calothrix*, which constructed many of the mats evident in samples from LY-2 and LY-3 (Fig. 7A-C). Characteristic features of these filaments include their basal heterocyst (Fig. 7B, C), large diameter (up to 10 μm) filaments, and the presence of a laminated sheath. In some areas, the mats are formed largely of interwoven filamentous microbes that may belong to the form-genus *Microcoleus*, which has a helical filament (up to 2 μm diameter) that is formed of numerous trichomes (up to 0.2 μm diameter). Rarer filamentous microbes that are locally intermixed with the *Calothrix* or *Microcoleus*?, include the form-genera *Phormidium* (Fig. 7H) and *Oscillatoria* (Fig. 7I, J). Bacteriform microbes, up to 500 nm long and 200 nm diameter, are scattered throughout many of the samples (Fig. 7K).

Some opal-A laminae have local concentrations of well-preserved diatoms (Fig. 7L-N) and scattered testate amoebae (Fig. 7O). Silicified and/or calcite-encrusted grass stems and leaves (broken stems and in growth position) are present in some laminae.

Si and Fe Precipitates. – Precipitates found in the deposits at springs Stjáni, LY-2, and LY-3 include opal-A, Fe-rich opal-A, and Fe-reticulate coatings (Fig 8).

Opal-A and Fe-rich opal-A.– Opal-A beads, up to 500 nm in diameter, are commonly associated with the biofilms, where they are embedded in or lie on top of the EPS (Figs. 6C, D, 8A, B). Many of the filamentous microbes are encased by opal-A beads, each up to 2 μm long (Fig. 8C, D). EDX analyses show that the Fe content of the beads varies from a trace to significant amounts, as judged from the height of the intensity peak for Fe on EDX analyses.

There is no recognizable pattern to Fe distribution because neighboring beads commonly contain significantly different amounts of Fe. Many of the Fe-rich opal beads, however, have a microscopically irregular surface unlike the smoother surfaces that typify Fe-poor opal-A spheres.

Si-Fe reticulate coatings.– The Si-Fe reticulate coatings form small clusters or coat various substrates (Fig. 8E, F). Although the Si-Fe-reticulate coating is less common than the Fe-rich opal-A beads, the two precipitates commonly occur together.

The Si-Fe reticulate coatings are morphologically similar to reticulate coatings that have been reported from various springs in Yunnan Province, China (Jones and Peng 2014b, 2016a), the Kenya Rift Valley (Casanova and Renaut 1987; Jones and Renaut 1996b, a), and New Zealand (Jones et al. 2003). Although Mg and Si are the dominant elements in these examples, other elements, including Fe, are commonly presence in lesser amounts. The origin of these coatings and the reasons for their highly variable compositions is still open to debate (Jones and Peng 2016a).

Calcite

Classification of the different types of calcite crystals found in the spring deposits at Lýsuhóll is difficult because (1) most of the crystals are not fully developed and their ultimate crystal form is not always evident, or (2) the morphology of the nanocrystals and mesocrystals and nanocrystals are variable at all scales (Figs. 9–17). For the purposes of description, the crystals are herein described according to two criteria. First, the crystals are described as (1) attached crystals that (a) nucleated upon and grew from a firm substrate, and (b) those that began as unattached crystals that probably grew within a biofilm and therefore show no evidence of growing from a substrate. Second, the calcite crystals are divided by their general crystal morphology into prismatic – types I, II, and III (Figs. 9, 10, 11, respectively), trigonal (Fig. 12), dodecahedrons (Fig. 13A–C), platy (Fig. 13D–F), rhombic – types I, II, and III (Figs. 14, 15, 16, respectively), and dendritic (Fig. 17).

Prismatic mesocrystals – Type I.– Small clusters of prismatic crystals, which typically formed small mounds rich in microbes and EPS (Fig. 4H), were found on the distal parts of the discharge aprons of LY-2 and LY-3. Although the individual mesocrystals, which are up to 500 μm long and 75 μm wide, are clearly elongate, they have not developed clearly defined facets (Fig. 9A, B). All of the crystals in these clusters are formed of rhombic nanocrystals that are of variable size (Fig. 9C–I). The development and internal structures of these nanocrystals is highly variable even among crystals that are part of the same cluster.

In some mesocrystals, 'blocky' nanocrystals are up to 1.5 μm long, 0.75 μm wide and 0.5 μm thick, and are perfectly aligned relative to each other in a clear crystallographic register (Fig. 9D–F). Individual nanocrystals range from perfectly formed blocks with smooth faces and well-defined crystal edges and corners (Fig. 9F) to blocky forms that are incompletely developed with at least one corner and parts of associated crystal faces poorly developed (Fig. 9D, E). With these nanocrystals, the same corner is always missing (Fig. 9D–F) and it is therefore assumed that it is a growth feature because it is difficult to envisage a dissolution process that would preferentially attack the same corner of every crystal.

Other mesocrystals from the same crystal cluster are formed of blocky to rhombic nanocrystals that are themselves formed of even smaller crystals (Fig. 9G–I). Thus, the largest nanocrystals, which are up to 3 μm long, 2 μm wide, and 0.75 μm thick, are built from smaller units with the same morphology but are up to 0.5 μm long and commonly < 0.25 μm long (Fig.

9J). All the nanocrystals, irrespective of size, align along the same crystallographic register (Fig. 9G–I).

Prismatic mesocrystals – Type II.– These crystals, which form small clusters that grow from a substrate, were found in the deposits from Stjáni, where they developed in the microbial mats (Fig. 10). Type II prismatic crystals, in common with Type I prismatic crystals, are incomplete in morphology and it is therefore difficult to define a precise crystallographic form (Fig. 10C). They differ from the Type I crystals because their constituent nanocrystals have a significantly different morphology from the latter. The Type II mesocrystals are formed of rhombic-shaped plates that are generally < 1 μm long and lie flat on earlier formed crystal faces. This arrangement creates an upward-expanding asymmetrical diamond-shaped structure that is formed of overlapping plate-like nanocrystals (Fig. 10A–D). The cross-section, which is perpendicular to the crystal face, is wedge-shaped with widest part pointing to the top of the mesocrystals (Fig. 10C).

Some of these crystals are decorated by flat, round to pentagonal nanocrystals (up to 5 μm long) with some being formed of smaller, irregular-shaped units (Fig. 10E). These crystals do not seem to be genetically linked to the Type II prismatic crystals.

Prismatic mesocrystals – Type III.– These mesocrystals are found in microbial mats on the middle and distal parts of the discharge aprons of springs LY-2 and LY-3. Small clusters in these mats are formed of crystals that are up to 200 μm long and 50 μm wide (Fig. 11A). The exact morphology of each crystal is difficult to define because the crystals are incompletely formed (Fig. 11). Some appear to be nearly hexagonal in cross-section whereas others are almost trigonal in form (Fig. 11E, F).

The constituent nanocrystals are less well defined than those that form Types I and II prismatic crystals. In most examples, the internal structure of these crystals approaches that of a three-dimensional dendrite with two sets of branches extending from a main branch (Fig. 11C, D). Although incompletely developed, these crystals terminate in smooth crystal faces that are typical of spar calcite crystals (Fig. 11B).

Trigonal mesocrystals.– Trigonal prismatic crystals, up to 250 μm long with sides up to 30 μm wide, grew from a nucleation site on a substrate. They are common in some of the samples from Stjáni and LY-3 (Fig. 12). These crystals are formed of nanocrystals of the same morphology, but with sides that are up to 10 μm long (Fig. 12F), but are typically < 3 μm wide (Fig. 12B–D). All of these nanocrystals share a common crystallographic register (Fig. 12). Filamentous microbes and/or EPS are associated with all of these crystals (Fig. 12C) and in many examples the crystals are difficult to assess morphologically because they are largely covered with EPS (Fig. 8I).

These trigonal mesocrystals are morphologically akin to similar crystals described and illustrated by Chafetz et al. (1985, their Fig. 6), Chafetz and Butler (1980, their Fig. 16), Jones and Renaut (1996c, their Fig. 3; 2008, their Fig. 9H), Rogerson et al. (2008, their Fig. 2), and Pedley et al. (2009, their Fig. 7C).

Dodecahedral mesocrystals.– These unattached crystals, which are characterized by twelve five-sided crystal faces, are scattered throughout the benthic microbial mats in the outflow from Stjáni spring (Fig. 13A–C). Their crystal faces and edges are poorly developed with many of the crystals having rounded edges. High-magnification SEM views of the crystals show that they are formed of small, plate-like nanocrystals that are generally < 1 μm long (Fig. 13C).

These dodecahedral crystals are morphologically akin to similar crystals described and illustrated by Jones and Peng (2014b, their Fig. 5A, B; 2014a, their Fig. 12B-E; 2016b, their Fig. 11A-C).

Platy mesocrystals.– These platy mesocrystals, found in some of the microbial mats from LY-2, are difficult to precisely define and describe because most of the crystals are incompletely developed (Fig. 13D–F). Most crystals, which appear to be rhombic in form, are up to 2.5 μm long, 2.0 μm wide, and < 0.5 μm thick. All of these crystals are formed of nanocrystals that are < 1 μm long with most < 0.5 μm long. Within any field of view on the SEM, all of the mesocrystals have their long axes in the same orientation (Fig. 13E–F), and vary from being widely dispersed to densely packed (Fig. 13D). In most cases these mesocrystals appear to be growing in biofilms and filamentous microbes are locally evident (Fig. 13D, E).

Rhombic mesocrystal – Type I.– The three types of rhombic crystals (Figs. 14–16) are incompletely developed and it is therefore difficult to delineate their morphology. Their description as ‘rhombic’ crystals is based on the overall morphology of the crystals and the general morphology of their constituent nanocrystals. Most of these crystals appear to be unattached to the substrate and probably developed within the confines of biofilms.

Type I rhombic mesocrystals were found in samples from the distal part of the discharge apron of spring LY-2 (Fig. 14). These mesocrystals, up to 100 μm long, are formed of nanocrystals that are up to 2 μm long, but mostly < 1 μm long (Fig. 14). The nanocrystals, characterized by smooth faces and well-defined crystal edges (Fig. 14B, C), are loosely packed with narrow (< 100 nm) gaps between adjacent crystals (Fig. 14C). All nanocrystals, irrespective of size, are in the same crystallographic register.

Rhombic mesocrystal – Type II.– Type II rhombic mesocrystals came from the middle part of the discharge apron of spring LY-2 (Fig. 15). Many of these crystals have well-defined crystallographic morphologies with many crystals displaying smooth, well-developed crystals edges and corners (Fig. 15B, D, E) and in some cases, well-developed smooth crystal faces (Fig. 15G–I). Rare crystals have completely developed, smooth crystal faces, edges, and corners (Fig. 15G, I). The nanocrystals that formed these crystals are readily apparent in any crystal that lacks smooth crystal faces (Fig. 15B–H). Most of the nanocrystals have a poorly developed, blocky appearance (Fig. 15B–H). There is no systematic distribution to these variably developed crystals with completely and incompletely formed crystals commonly occurring within microns of each other (Fig. 15G).

Rhombic mesocrystal – Type III.– Type III rhombic mesocrystals, up to 2 μm long, are formed of overlapping rhombic-shaped plates (Fig. 16) that are similar to the nanocrystals evident in the Type II prismatic calcite crystals. Oblique views of these nanocrystals show that they seem to be formed of a series of nested plates with each having rims that are slightly more prominent than their interiors (Fig. 16B–D). In cross-section, the plates are wedge-shaped and commonly display serrated edges due to the elevated rims of the constituent nanocrystals (Fig. 16D, E). All of the nanocrystals have a common crystallographic register (Fig. 16). This is readily apparent on crystal faces where the nested rhombic nanocrystals are all perfectly aligned (Fig. 16E, F).

The nanocrystals evident in these rhombic mesocrystals are morphologically similar to the "overlapping rhombus shaped scales" evident in some of the subhedral calcite crystals that Turner and Jones (2005, their Fig. 6) documented from Big Hill Springs in Alberta, Canada. The wedge-shaped cross-sectional form in those crystals (Turner and Jones 2005, their Fig. 6D) is identical to the nanocrystals in the crystals from Lýsuhóll (Fig. 16C, D).

Calcite dendrites.– Some of the samples from LY-2 contain calcite dendrites that are characterized by three main branches, each up to 1 μm long and generally < 200 nm wide, which are at 90–100° to each other (Fig. 17). In some dendrites, smaller branches grow from the main branches (Fig. 17D). All the dendrites have a common orientation (Fig. 17).

These dendrites are morphologically similar to the calcite dendrites that Turner and Jones (2005, their Figs. 4D, 5) described and illustrated from Big Hills Springs in Alberta, Canada. In those examples, some of the dendrites defined a triangular shape with the three arms of the dendrite extending to the corners of the triangle. In areas where the dendrites were closely packed, the triangular form was difficult to delineate, in common with the examples from Lýsuhóll.

DISCUSSION

Spring precipitates from Lýsuhóll are formed of opal-A (Fig. 6C, D), Fe-rich opal-A (Figs. 5, 8A–D), Fe-rich reticulate coatings (Fig. 8E, F), and various types of calcite crystals (Figs. 9–17) that are intermixed at all scales. In some samples, these phases are segregated into distinct laminae (Fig. 5), whereas in other samples, the opal-A, Fe-rich precipitates, and calcite are intimately related on a microscale (Fig. 8G, I). The compositional contrast is accentuated because many microbes in the Lýsuhóll samples have been well preserved through silicification (Fig. 7) but there is little evidence of microbial calcification. Similarly, no evidence of microbially entombment, as described by (Melim et al. 2016), was found in these deposits. The silicification, which must have occurred rapidly before the microbes decayed (Jones et al. 2004), is similar to that seen in thermal spring deposits throughout the world (e.g., Cady and Farmer

1996; Jones et al. 1998; Renaut et al. 1998; Konhauser et al. 1999; Jones et al. 2003). Rapid precipitation of opal-A and Fe-rich opal-A is also evident where these precipitates are intimately associated with thin films of EPS that stretch between neighboring microbes (Fig. 6D, E). The general paucity of calcified microbes and EPS in the Lýsuhóll spring deposits is typical of travertine and tufa found in many other modern hot springs (e.g., Jones and Renaut 1995; Peng and Jones 2012).

Calcite crystals forming in hot-spring systems can develop by classical or non-classical crystal-growth models. The classical growth model involves atom-by-atom additions to a nucleus (Geng et al. 2010). In contrast, non-classical crystal growth is a particle-based system (Cölfen and Antonietti 2005; Meldrum and Cölfen 2008; Geng et al. 2010) in which mesocrystals grow through the oriented attachment of nanocrystals (Niederberger and Cölfen 2006, their Fig. 1). Although growth mechanisms are debated, they may involve (1) an organic matrix with oriented compartments where crystalline matter forms and/or promotes alignment, (2) physical fields or mutual alignment of crystal faces, (3) epitaxial growth with mineral bridging between neighboring nanocrystals, and/or (4) alignment by spiral constraints (Song and Cölfen 2010).

Bacterial shrubs, formed of calcite and Fe- and/or Mn-rich minerals, are common features of many hot-water travertine deposits (Chafetz and Meredith 1983; Folk and Chafetz 1983; Chafetz and Folk 1984; Chafetz et al. 1998; Chafetz and Guidry 1999). According to Chafetz and Guidry (1999), the bacteria create microenvironments around their colonies where mineral precipitation takes place. Although common in hot-water travertine deposits, bacterial shrubs have not been found in low-temperature systems (Chafetz and Guidry 1999, p. 58). No evidence of bacterial shrubs was found in the precipitates associated with the springs at Lýsuhóll.

As outlined by Ronholm et al. (2014), mineral precipitation associated with microbial biofilms may result from (1) metabolic processes (e.g., photosynthesis, urea hydrolysis), (2) the presence of nucleation sites on cell surfaces (e.g., proteins, lipids), and/or (3) the EPS that can trap and concentrate cations (e.g., Braissant et al. 2007; Braissant et al. 2009). The physiochemical environment that develops in the EPS controls the polymorph that forms and its crystal morphology (Kawaguchi and Decho 2002; Braissant et al. 2003; Dupraz et al. 2009). Laboratory experiments that have used hydrogels to mimic EPS have shown the impact that the medium can have on calcite precipitation and growth of mesocrystals (e.g., Falini et al. 2000; Li and Estroff 2007; Nindiyasari et al. 2014). Nevertheless, recognition of bacterially-induced precipitates in natural samples other than bacterial shrubs has been a subject of much debate (e.g., Chekroun et al. 2004).

All calcite crystals in the spring deposits at Lýsuhóll are mesocrystals that grew from nanocrystals aligned along perfect crystallographic registers (Figs. 9–17). In the field, microbial mats clearly covered the discharge aprons at Stjáni, LY-2, and LY-3 (Figs. 2B, C, 3 and 4) in summer 2005. Samples from those aprons show evidence of filamentous microbes and their associated EPS. There is evidence, therefore, that the calcite crystals grew within microbial mats (Fig. 6A–D). This is supported by growth of crystals unattached to a substrate (Fig. 13A–C).

At Big Hills Springs, Alberta, Canada, calcite forming on bryophyte ‘leaves’ includes dendrites similar to those at Lýsuhóll (Fig. 17) and other subhedral crystals (Turner and Jones 2005, their Figs. 4-8). Many subhedral crystals illustrated by Turner and Jones (2005, their Figs. 6, 7, 8A) are redefined here as mesocrystals built from well-defined nanocrystals. The wedge-shaped platy nanocrystals in some Lýsuhóll mesocrystals (Figs. 16C, D) are, for example, identical in morphology to some nanocrystals found in many mesocrystals from Big Hills Springs (Turner and Jones 2005, their Fig. 6D). Turner and Jones (2005) argued that the dendrites and mesocrystals on the bryophyte leafs formed in the negatively-charged EPS films that coat the bryophyte leafs where higher saturation levels with respect to $CaCO_3$ developed in sites of rapid CO_2 degassing in splashing water. They also argued that the calcite crystals nucleated in biofilms because calcareous substrates for heterogeneous nucleation and growth were rare. Similar criteria apply to the calcite crystals growing at Lýsuhóll.

In modern samples, mesocrystals might indicate crystal growth in biofilms. In older spring deposits, however, recognition of calcite mesocrystals might be difficult for many reasons:

- Fusion of nanocrystals will transform mesocrystals to monocrystals that cannot be distinguished from a monocrystal that grew by the classical crystal-growth model.
- Evidence of biofilms in which calcite crystals grew will disappear quickly because of the low preservation potential of the microbes and their associated EPS. Although samples from Lýsuhóll were covered by biofilms when collected, only scattered, poorly preserved filamentous microbes and patches of EPS were seen when they were examined soon after collection (within 3 months). The exception was in localized areas where microbial mats had been silicified.
- Most mesocrystals from the Lýsuhóll springs are < 1 mm long; many are < 0.5 mm long. Had precipitation continued, these crystals would have become nucleation centers for

growth of larger crystals. If that growth occurred by the classical crystal-growth model evidence of the mesocrystal phase would have been lost.

For spring systems, the precipitation of the different $CaCO_3$ polymorphs and crystal morphogenesis has been attributed to many different factors that operate at all scales (Jones 2017a, b). In many cases, precipitation is linked directly to the temperature and chemical properties of the spring water. Folk (1994, his Fig. 2), for example, argued that (1) aragonite forms where the water T > 40–45°C, regardless of fluid composition, (2) if the Mg:Ca molar ratio is > 1:1, aragonite forms regardless of water T, and (3) calcite forms if T < 40°C and the water is Ca-rich relative to Mg. Critically, however, he added two exceptions, namely (1) in areas with rapid CO_2 degassing, aragonite will form even where conditions favor calcite precipitation, and (2) if ion transfer is low because of viscous fluids or mucal films, calcite might form even in hot waters (Buczynski and Chafetz 1991). Pentecost (2005, his Fig. 37) also used a similar approach. This approach, however, largely ignores the fact that biofilms effectively isolate substrates and spring precipitates from the surrounding water (Decho and Lopez 1993; Decho 2000, 2010). If calcite precipitates in microbial mats it becomes difficult to correlate that precipitation directly with the physiochemical properties of the spring water, including vent T and pH. This was clearly demonstrated by Peng and Jones (2013) who showed that amorphous calcium carbonate (ACC), calcite, and aragonite were forming in neighboring microdomains in microbial mats in Eryuan hot springs (Yunnan Province, China). Such variance in the precipitates was attributed to the different physiochemical conditions that existed in each microdomain (Peng and Jones 2013), which were also different from those in the ambient flowing spring water.

CONCLUSIONS

Analyses of samples from the discharge aprons of three springs at Lýsuhóll, Iceland, have led to the following conclusions:

- Precipitates forming on the modern discharge aprons include opal-A, Fe-rich opal-A, Fe-rich reticulate coatings, and calcite, that are intermixed at all microscales.
- Precipitation of some mineral phases was mediated by ubiquitous biofilms.
- Although some resident microbes were preserved through silicification, none were preserved by calcification.
- A variety of calcite crystal morphologies developed within the biofilms that coat substrates in the spring outflow pools and channels. In many examples, contrasting crystal morphologies developed within neighboring microdomains within the biofilms.
- Different calcite mesocrystals evolved through the oriented attachment of nanocrystals that occurred within the biofilms.

It is difficult to recognize mesocrystals because their identity might be lost during the fusion when constituent nanocrystals transform to monocrystals which appear identical to monocrystals that developed by the classical crystal-growth mechanism. This problem is compounded because the original microbial mats might not be preserved, given that their preservation potential in a carbonate system is low. Any assessment of the precipitation of calcite in spring systems must include the possibility that non-classical crystal growth took place in the microdomains that characterize the biofilms.

ACKNOWLEDGEMENTS

This research was made possible by funding from the Natural Sciences and Engineering Research Council of Canada (grants G04246 to Jones and GP0629 to Renaut). We are indebted to the land owners who gave us permission to examine the springs and collect the samples needed for this study. We are also indebted to George Braybrook who took most of the SEM images used in this paper. We are also indebted to Editor Dr. L. Melim, Associate Editor Dr. K. Benison, and reviewers Drs. H. Chafetz and M. Gradzinski for their constructive criticisms of an earlier version of this manuscript.

REFERENCES

ARNÓRSSON, S., AND BARNES, I., 1983, The nature of carbon dioxide waters in Snæfellsnes, western Iceland: Geothermics, v. 12, p. 171-176.

BARTH, T.F.W., 1950, Volcanic geology, hot springs and geysers of Iceland, Publication 587: Washington, Carnegie Institution of Washington, 174 p.

BINKLEY, K.L., WILKINSON, B.H., AND OWEN, R.M., 1980, Vadose beachrock cementation along a southeastern Michigan marl lake: Journal of Sedimentary Petrology, v. 50, p. 953-962.

BRAISSANT, O., CAILLEAU, G., DUPRAZ, C., AND VERRECCHIA, E.P., 2003, Bacterially induced mineralization of calcium carbonate in terrestrial environments: the role of exopolysaccharides and amino acids: Journal of Sedimentary Research, v. 73, p. 485-490.

BRAISSANT, O., DECHO, A.W., DUPRAZ, C., GLUNK, C., PREZEKOP, K.M., AND VISSCHER, P.T., 2007, Exopolymeric substances of sulphate-reducing bacteria: interactions with calcium at alkaline pH and implication for formation of carbonate minerals: Geobiology, v. 5, p. 401-411.

BRAISSANT, O., DECHO, A.W., PRZEKOP, K.M., GALLAGHER, K.L., GLUNK, C., DUPRAZ, C., AND VISSCHER, P.T., 2009, Characteristics and turnover of exoplymeric substances in a hypersaline microbial mat: FEMS Microbiology Ecology, v. 67, p. 293-307.

BUCZYNSKI, C., AND CHAFETZ, H.C., 1991, Habit of bacterially induced precipitates of calcium carbonate and the influence of medium viscosity on mineralogy: Journal of Sedimentary Petrology, v. 61, p. 221-233.

CADY, S.L., AND FARMER, J.D., 1996, Fossilization processes in siliceous thermal springs: trends in preservation along thermal gradients, *in* Bock, G.R., and Goode, J.A., eds., Evolution of

Hydrothermal Ecosystems on Earth (and Mars?). Ciba Foundation Symposium: Chichester, U.K., Wiley, p. 150-173.

CASANOVA, J., AND RENAUT, R.W., 1987, Les stromatolites du milieu hydrothermal, *in* Tiercelin, J.J., and Vincens, A., eds., Le demi-graben de Baringo-Bopgoria, Rift Gregory, Kenya: 30,000 ans d'histoire hydrologique et sédimentaire, Centres de Recherches Exploration-Production Elf-Aquitaine, p. 484-490.

CHAFETZ, H.S., AKDIM, B., JULIA, R., AND REID, A., 1998, Mn- and Fe-rich black travertine shrubs: bacterially (and nanobacterially) induced precipitates: Journal of Sedimentary Research, v. 68, p. 404-412.

CHAFETZ, H.S., AND BUTLER, J.C., 1980, Petrology of recent caliche pisolites, spherulites and speleothem deposits from central Texas: Sedimentology, v. 27, p. 407-518.

CHAFETZ, H.S., AND FOLK, R.L., 1984, Travertines: depositional morphology and the bacterially constructed constituents: Journal of Sedimentary Petrology, v. 54, p. 289-316.

CHAFETZ, H.S., AND GUIDRY, S.A., 1999, Bacterial shrubs, crystal shrubs, and ray-crystal shrubs: bacterial vs. abiotic precipitation: Sedimentary Geology, v. 126, p. 57-74.

CHAFETZ, H.S., AND MEREDITH, J.S., 1983, Recent travertine pisoliths (pisoids) from southeastern Idaho, U. S. A., *in* Peryt, T.M., ed., Coated Grains: Berlin, Springer-Verlag, p. 450-455.

CHAFETZ, H.S., WILKINSON, B.H., AND LOVE, K.M., 1985, Morphology and composition of non-marine carbonate cements in near-surface settings, *in* Schneidermann, N., and Harris, P.M., eds., Carbonate Cements, Society of Economic Paleontologists and Mineralogists, Special Publication 36, p. 337-347.

CHEKROUN, K.B., RODRÍGUES-NAVARRO, C., GONZÁLEZ-MUÑOZ, M.T., ARIAS, J.M., CULTRONE, G., AND RODRÍGUEZ-GALLEGO, M., 2004, Precipitation and growth morphology of calcium carbonate induced by *Myxococcus xanthus:* implications for recognition of bacterial carbonates: Journal of Sedimentary Research, v. 74, p. 868-876.

CÖLFEN, H., AND ANTONIETTI, M., 2005, Mesocrystals: inorganic superstructures made by highly parallel crystallization and controlled alignment: Angewandte Chemie, v. 44, p. 5576-5591.

DECHO, A.W., 2000, Microbial biofilms in intertidal systems: an overview: Continental Shelf Research, v. 20, p. 1257-1273.

DECHO, A.W., 2010, Overview of biopolymer-induced mineralization: what goes on in biofilms?: Ecological Engineering, v. 36, p. 137-144.

DECHO, A.W., AND LOPEZ, G.R., 1993, Exopolymer microenvironments of microbial flora: multiple and interactive effects on trophic relationships: Limnology and Oceanography, v. 38, p. 1633-1645.

DUPRAZ, C., REID, R.P., BRAISSANT, O., DECHO, A.W., NORMAN, R.S., AND VISSCHER, P.T., 2009, Processes of carbonate precipitation in modern microbial mats: Earth-Science Reviews, v. 96, p. 141-162.

EINARSSON, Þ., 1994, Geology of Iceland: Reykjavík, Mál og menning, 309 p.

FALINI, G., FERMANI, S., GAZZOANO, M., AND RIPAMONTI, A., 2000, Polymorphism and architectural crystal assembly of calcium carbonate in biologically inspired polymeric matrices: Journal of Chemical Society - Dalton Transactions, v. 21, p. 3983-3987.

FOLK, R.L., 1994, Interaction between bacteria, nannobacteria, and mineral precipitation in hot springs of central Italy: Géographie physique et Quaternaire, v. 48, p. 233-246.

FOLK, R.L., AND CHAFETZ, H.S., 1983, Pisoliths (pisoids) in Quaternary travertines of Tivoli, Italy, *in* Peryt, T.M., ed., Coated Grains: Berlin Heidelberg, Springer-Verlag, p. 474-487.

FRIÐLEIFSSON, G.Ó., 1992, Thoughts on geothermal energy in Snæfellnes, Orkustofnun, report, OS-GÓF-91/01: Reykavík, Orkustofnun (in Icelandic).

FRIÐLEIFSSON, G.Ó., AND ÁRMANNSSON, H., 1999, Silica sinters at Snaefellnes and Hnappadalur, west Iceland, *in* Ármannsson, H., ed., Geochemistry of the Earth's Surface: Rotterdam, Balkema, p. 499-502.

GENG, X., LIU, L., JIANG, J., AND YU, S.-H., 2010, Crystallization of $CaCO_3$ mesocrystals and complex aggregates in a mixed solvent media using polystyrene sulfonate as a crystal growth modifier: Crystal Growth and Design, v. 10, p. 3448-3453.

GIVEN, R.K., AND WILKINSON, B.H., 1985, Kinetic control of morphology, composition and mineralogy of abiotic sedimentary carbonates: Journal of Sedimentary Petrology, v. 55, p. 109-119.

JÓHANNESSON, H., AND SÆMUNDSSON, K., 1998, Jarðfræðikort af Íslandi 1:500 000: Berggrunnur. (2. Útgáfa). (Geological Map of Iceland 1:500,000: Bedrock geology, 2nd Edition): Náttúrufræðistofnun Íslands.

JONES, B., 1989, Syntaxial overgrowths on dolomite crystals in the Bluff Formation, Grand Cayman, British West Indies: Journal of Sedimentary Petrology, v. 59, p. 839-847.

JONES, B., 2017a, Review of aragonite and calcite crystal morphogenesis in thermal spring systems: Sedimentary Geology, v. 354, p. 9-23.

JONES, B., 2017b, Review of calcium carbonate polymorph precipitation in spring systems: Sedimentary Geology, v. 353, p. 64-75.

JONES, B., AND PENG, X., 2012, Amorphous calcium carbonate associated with biofilms in hot springs: Sedimentary Geology, v. 269-270, p. 58-68.

JONES, B., AND PENG, X., 2014a, Hot spring deposits on a cliff face: a case study from Jifei, Yunnan Province, China: Sedimentary Geology, v. 302, p. 1-28.

JONES, B., AND PENG, X., 2014b, Signatures of biologically influenced $CaCO_3$ and Mg-Fe silicate precipitation in hot springs: case study from the Ruidian geothermal area, Western Yunnan Province, China: Sedimentology, v. 61, p. 56-89.

JONES, B., AND PENG, X., 2016a, Growth and development of spring towers at Shiqiang, Yunnan Province, China: Sedimentary Geology, v. 347, p. 183-209.

JONES, B., AND PENG, X., 2016b, Mineralogical, crystallographic, and isotopic constraints on the precipitation of aragonite and calcite at Shiqiang and other hot springs in Yunnan Province, China: Sedimentary Geology, v. 345, p. 103-125.

JONES, B., AND RENAUT, R.W., 1995, Noncrystallographic dendrites from hot-spring deposits at Lake Bogoria, Kenya: Journal of Sedimentary Research, v. A65, p. 154-169.

JONES, B., AND RENAUT, R.W., 1996a, Influence of thermophilic bacteria on calcite and silica precipitation in hot springs with water temperatures above 90°C: evidence from Kenya and New Zealand: Canadian Journal of Earth Sciences, v. 33, p. 72-83.

JONES, B., AND RENAUT, R.W., 1996b, Morphology and growth of aragonite crystals in hot-spring travertines at Lake Bogoria, Kenya Rift Valley: Sedimentology, v. 43, p. 323-340.

JONES, B., AND RENAUT, R.W., 1996c, Skeletal crystals of calcite and trona from hot-spring deposits in Kenya and New Zealand: Journal of Sedimentary Research, v. 66, p. 265-274.

JONES, B., AND RENAUT, R.W., 2008, Cyclic development of large, complex calcite dendrite crystals in the Clinton travertine, Interior British Columbia, Canada: Sedimentary Geology, v. 203, p. 17-35.

JONES, B., RENAUT, R.W., OWEN, R.B., AND TORFASON, H., 2005, Growth patterns and implications of complex dendrites in calcite travertines from Lýsuhóll, Snæfellsnes, Iceland: Sedimentology, v. 52, p. 1277-1301.

JONES, B., RENAUT, R.W., AND ROSEN, M.R., 1998, Microbial biofacies in hot-spring sinters: a model based on Ohaaki Pool, North Island, New Zealand: Journal of Sedimentary Research, v. 68, p. 413-434.

JONES, B., RENAUT, R.W., AND ROSEN, M.R., 2003, Silicified microbes in a geyser mound: the enigma of low-temperature cyanobacteria in a high-temperature setting: Palaios, v. 18, p. 87-109.

JONES, B., RENAUT, R.W., AND ROSEN, M.R., 2004, Taxonomic fidelity of silicified microbes from hot spring systems in the Taupo Volcanic Zone, North Island, New Zealand: Transactions of the Royal Society of Edinburgh: Earth Sciences, v. 94, p. 475-483.

KAWAGUCHI, T., AND DECHO, A.W., 2002, A laboratory investigation of cyanobacterial extracellular polymeric secretions (EPS) in influencing $CaCO_3$ polymorphism: Journal of Crystal Growth, v. 240, p. 230-235.

KHARAKA, Y.K., GUNTHER, W.D., AGGARWAL, P.K., PERKINS, E.H., AND DEBRAAL, J.D., 1988, SOLMINEQ.88. A computer program for geochemical modeling of water-rock interactions, USGS Water Resources Investigations Report 88-4227.

KJARTANSDÓTTIR, R., 2014, Carbon isotopes and systematics of Icelandic low-temperature geothermal waters [unpublished M.Sc. thesis]: Univesity of Iceland, Iceland, 39 p.

KJARTANSSON, G., 1947, Travertines in Iceland: Náttürufrædingurinn, v. 17, p. 88-92 (in Icelandic).

KONHAUSER, K.O., AND FERRIS, F.G., 1996, Diversity of iron and silica precipitation by microbial mats in hydrothermal waters, Iceland: implications for Precambrian iron formations: Geology, v. 24, p. 323-326.

KONHAUSER, K.O., PHOENIX, V.R., BOTTRELL, S.H., ADAMS, D.G., AND HEAD, I.M., 1999, Microbial-silica interactions in modern hot spring sinter, *in* Armannsson, H., ed., Geochemistry of the Earth's Surface: Rotterdam, A.A. Balkema, p. 263-266.

LI, H., AND ESTROFF, L.A., 2007, Porous calcite single crystals grown in a hydrogel medium: CrystEngComm, v. 9, p. 1153-1155.

MELDRUM, F.C., AND CÖLFEN, H., 2008, Controlling mineral morphologies and structures in biological and synthetic systems: Chemical Reviews, v. 108, p. 4332-4432.

MELIM, L.A., NORTHUP, D.E., BOSTON, P.J., AND SPILDE, M.N., 2016, Preservation of fossil microbes and biofilm in cave pool carbonates and comparison to other microbial carbonate environments: Palaios, v. 31, p. 177-189.

NIEDERBERGER, M., AND CÖLFEN, H., 2006, Oriented attachment and mesocrystals: non-classical crystallization mechanisms based on nanoparticle assembly: Physical Chemistry Chemical Physics, v. 8, p. 3271-3287.

NINDIYASARI, F., FERNÁNDEZ-DÍAZ, L., GRIESSHABER, E., ASTILLEROS, J.M., SÁNCHEZ-PASTOR, N., AND SCHMAHL, W.W., 2014, Influence of gelatin hydrogel porosity on the crystallization of $CaCO_3$: Crystal Growth and Design, v. 14, p. 1531-1542.

Owen, R.B., Renaut, R.W., and Jones, B., 2008, Geothermal diatoms: a comparative study of floras in hot spring systems of Iceland, New Zealand, and Kenya: Hydrobiologia, v. 610, p. 175-192.

Pedley, M., Rogerson, M., and Middleton, R., 2009, Freshwater calcite precipitates from in vitro mesocosm flume experiments: a case for biomediation of tufas: Sedimentology, v. 56, p. 511-527.

Peng, X., and Jones, B., 2012, Rapid precipitation of silica (opal-A) disguises evidence of biogenicity in high-temperature geothermal deposits: case study from Dagunguo hot spring, China: Sedimentary Geology, v. 257-258, p. 45-62.

Peng, X., and Jones, B., 2013, Patterns of biomediated $CaCO_3$ crystal bushes in hot spring deposits: Sedimentary Geology, v. 294, p. 105-117.

Pentecost, A., 2005, Travertine: Berlin Heidelberg, Springer, 445 p.

Pentecost, A., 2011, Some observations on travertine algae from Stjáni hot spring, Lýsuhóll, Iceland: Nordic Journal of Botany, v. 29, p. 741-745.

Renaut, R.W., Jones, B., and Tiercelin, J.-J., 1998, Rapid *in situ* silicification of microbes at Loburu hot springs, Lake Bogoria, Kenya Rift Valley: Sedimentology, v. 45, p. 1083-1103.

Rogerson, M., Pedley, H.M., Wadhawan, J.D., and Middleton, R., 2008, New insights into biological influence on the geochemistry of freshwater carbonate deposits: Geochimica et Cosmochimica Acta, v. 72, p. 4976-4987.

Ronholm, D., Schumann, D., Sapers, H.M., Izawa, M., D., A., Berg, B., Mann, P., Vali, H., Flemming, R.L., Cloutis, E.A., and Whyte, L.G., 2014, A mineralogical characterization of biogenic calcium carbonates precipitated by heterotrophic bacteria isolated from cryophilic polar regions: Geobiology, v. 12, p. 542-556.

SANDBERG, P., 1985, Aragonite cements and their occurrence in ancient limestones, *in* Schneidermann, N., and Harris, P.M., eds., Carbonate Cements, Society of Economic Paleontologists and Mineralogists Special Publication No. 36, p. 33-57.

SIGURDSSON, H., 1970a, The petrogenesis and geochemistry of the Setberg volcanic region and of the immediate and acid rocks of Iceland: Durham, University of Durham, 321 p.

SIGURDSSON, H., 1970b, Structural origin and plate tectonics of the Snæfellsnes volcanic zone, western Iceland: Earth and Planetary Science Letters, v. 10, p. 129-135.

SONG, R.-Q., AND CÖLFEN, H., 2010, Mesocrystals – ordered nanoparticle superstructures: Advanced Materials, v. 22, p. 1301-1330.

TAZAKI, K., 1995, Electron microscopic observation of biomineralization in biomats from hot springs: Journal of the Geological Society of Japan, v. 101, p. 304-314.

TAZAKI, K., 1999, Architecture of biomats reveals history of geo-, aqua-, and bio-systems: Episodes, v. 22, p. 21-25.

TAZAKI, K., ISHIDA, H., AND FYFE, W.S., 1995, Calcite deposition in a hot spring microbial mat from Iceland: Clays: Controlling the Environment. 10th International Clay Conference, p. 30-37.

THOMAS, D.L., BIRD, D.K., ARNÓRSSON, S., AND MAHER, K., 2016, Geochemistry of CO_2-rich waters in Iceland: Chemical Geology, v. 444, p. 158-179.

TOWE, K.M., 1967, Echinoderm calcite: single crystal or polycrystalline aggregate: Science, v. 157, p. 1048-1050.

TULINIUS, H., HJARTARSON, Á., FRIÐLEIFSSON, G.Ó., AND SVERRISDÓTTIR, G., 1991, Hnappadalur – cold water and geothermal energy. A specialized fish farming project 1989-1990, Orkustofnun Report OS-91039/JHD-05): Reykavík, Iceland, Orkustofnun.

TURNER, E.C., AND JONES, B., 2005, Microscopic calcite dendrites in cold-water tufa: implications for nucleation of micrite and cement: Sedimentology, v. 52, p. 1043-1066.

WARING, G.A., 1965, Thermal springs of the United States and other countries of the world – A summary, United States Geological Survey Professional Paper 492, 383 p.

WHITE, D.E., HEM, J.D., AND WARING, G.A., 1963, Chapter F. Chemical composition of sub-surface waters: Geological Survey Professional Paper 440-F, p. F1-F67.

FIGURE CAPTIONS

FIG. 1.– **A)** Location of Lýsuhóll on Snæfellsnes Peninsula, west coast of Iceland. **B)** Location of Stjáni (LY-1) near Hrútsgill and springs LY-2 and LY-3 that are located in the nearby horse paddock.

FIG. 2.– **A)** General view of Lýsuhóll showing locations of Stjáni and springs LY-2 and LY-3 and locations LY-4 to LY-7 where additional water samples were collected. View looking to southeast. **B)** General view showing vent at spring LY-2 and triangular-shaped discharge apron. Letters a to f indicate locations where most samples were collected. **C)** General view of LY-3 showing spring vent and triangular-shaped discharge apron. Letters a to g indicate locations where most samples were collected. Temperatures (°C) of water at different locations at these two spring systems were measured on August 26, 2005.

FIG. 3.– The Stjáni spring system (LY-1). **A)** Panoramic view of spring showing location of spring, main spring pool, and discharge apron. Temperatures (°C) at different sites on the discharge apron were measured on August 26, 2005. White upper-case letters B, C, E, and G on black background indicate positions where images shown in panels B, C, E, and G were taken. Black lower-case letters a to k, on white backgrounds, indicate sample locations. **B)** Spring water piped to concrete surrounded pool. Note floating microbial mats (arrows) in spring water pools. **C)** Proximal part of discharge apron covered with thriving green microbial mat. **D)** Small channel on discharge apron with well-developed microbial mat formed largely of long filamentous streamers. **E)** Exposed part of discharge apron with low rimstone dams enclosing small rimstone pools. Note blades of grass coated with calcite crystals (arrows). **F)** Small, shallow pool on distal part of discharge apron with microbial mat covering floor and small, floating microbial mats (arrows) that are anchored around grass

stems. **G)** Small pool (cause by tire rut) with dendritic calcite bushes growing on floor. Note blades of grass.

FIG. 4.– Views of discharge aprons associated with springs LY-2 (A-D) and LY-3 (E-H). **A)** Proximal part of LY-2 system showing water flowing from vent along a narrow channel. Note red, Fe-rich precipitates on channel floor and green, microbial mats on channel margins. Hammer handle is 33 cm long. **B)** Upper part of channel from panel A, showing red, Fe-rich precipitates on channel floor and green, microbial mats along margins that are formed largely of long filamentous streamers. **C)** Middle part of discharge apron showing terraces formed by low rimstone dams around small rimstone pools. Most pools floored by loose carbonate sediment. **D)** Carbonate detritus on pool floor. **E)** Vent area of spring LY-3 showing red, Fe-rich precipitates covering pool floor. **F)** Middle part of discharge apron with terraces like those found on LY-2 (see panel C). **G)** Small rimstone pool with two thin-shelled gastropods surrounded by carbonate sediment. **H)** Distal part of discharge apron showing small mounds formed of clusters of calcite crystals enveloped by mucus and filamentous microbes.

FIG. 5.– SEM photomicrographs showing microscale relationships between laminae of different compositions. Elemental content determined by EDX analyses. Sample from locality 2a. **A)** Opal-A laminae (lower part) with silicified filamentous microbes (probably *Calothrix*) overlain by Fe-rich opal-A lamina that is formed largely of *Calothrix* that have been preserved by Fe-rich opal-A. **B)** Fe-rich opal-A laminae (with trace of Ca) sandwiched between two calcite laminae. **C)** Thin calcite laminae sandwiched between opal-A laminae.

FIG. 6.– SEM photomicrographs showing relationships between precipitates and microbial mats at Stjáni (S) and LY-2. The calcite crystals shown in panels A to D are held in the microbial mats and are not attached to a substrate. **A)** Layers of calcite crystals embedded in

filamentous microbial mat. Locality S-b. **B)** Small cluster of calcite crystals held in filamentous microbial mat. Locality S-e. **C)** Web formed of EPS stretched between filamentous microbes. Note small clusters of opal-A beads on surface of EPS and locally silicified filamentous microbes (SF). Locality S-j. **D)** Clusters of opal-A beads on surface of EPS mat. Locality LY-2e.

FIG. 7.– SEM photomicrographs of dominant silicified microbes found in deposits associated with springs LY-2 and LY-3. **A)** Basal part of filamentous microbial mat formed largely of *Calothrix*. Locality LY-2a. **B, C)** Basal parts of *Calothrix* filaments showing basal heterocyst. Locality LY-2a. **D)** Mat formed of helical filaments that are each formed of numerous trichomes, possibly *Microcoleus*. Locality LY-3c. **E, F)** Enlarged views of filaments, like those in panel D, showing helical spiral form and multiple trichomes. Localities LY-3c and LY-2a, respectively. **G)** View along axis of *Microcoleus*? showing its spiral form. Locality LY-2e. **H)** Scattered *Phormidium* (?) associated with *Microcoleus*(?).Locality LY-2d. **I, J)** *Oscillatoria* (?). Locality LY-2c. **K)** Silicified bacteriform microbes in EPS film. Locality LY-2b. **L–N)** Examples of well-preserved diatoms that are associated with the microbial mats. Localities LY-2a, 3e, and 3e, respectively. **O)** Testate amoeba. Locality LY-2c.

FIG. 8.– SEM photomicrographs of precipitates found at springs LY-2 and LY-3. Elemental content as determined by EDX analyses. **A, B)** Opal-A associated with EPS that contains various amounts of Fe. Localities LY-2a and 2c, respectively. **C)** Fe-rich opal-A coating filamentous microbe. Locality LY-3a. **D)** Enlarged view of Fe-rich opal-A beads from panel C. Locality LY-3a. **E, F)** Reticulate coatings formed of Si, Fe, and locally minor amounts of

Mn. Localities LY-2c and 3a, respectively. **G–I)** Examples of calcite crystals partly covered by EPS and opal-A beads. Locality 2e.

FIG. 9.– SEM photomicrographs of Prismatic Type I crystals from locality LY-2e. **A)** Cluster of crystals with strands of EPS on surfaces. White letter B indicates position of panel B. **B)** Cross-sectional shapes of upper parts of crystals in central part of cluster shown in panel A. White letter C indicates position of panel C. **C)** General view of crystal formed of perfectly aligned nanocrystals. **D–F)** Enlarged views of perfectly aligned nanocrystals from crystal shown in panel C. Note that some nanocrystals are perfectly formed with smooth faces whereas others are incompletely formed (arrows on panel D). **G)** Group of crystals from another cluster (like that shown in panel A) showing mesocrystals formed of aligned nanocrystals. White letter H indicates position of panel H. **H)** Surface of crystals showing perfectly aligned rhombic nanocrystals. White letter I indicates position of panel I. **I)** Example of nanocrystal formed of even smaller crystals that are of various sizes (arrows).

FIG. 10.– SEM photomicrographs of Prismatic Type II calcite crystals from Stjáni (S). **A)** Basal part of prismatic crystal. White letters B and C indicate positions of panels B and C, respectively. Locality S-b. **B)** Enlarged view of basal part of prismatic crystal showing surfaces formed of nested plate-like nanocrystals that are arranged in a common crystallographic register. Locality S-b. **C)** General view of small cluster of Prismatic Type II crystals. White letter D indicates position of panel D. Locality S-c. **D)** Side of prismatic crystal showing nested, rhombic-shaped nanocrystals. Locality S-c. **E)** Small irregular to rounded crystals on surface of prismatic crystals (arrows). Locality S-c.

FIG. 11.– Photomicrographs of Prismatic Type III calcite mesocrystals from distal parts of discharge aprons at springs LY-2 and LY-3. **A)** General view of upper part of prismatic

crystal. White letter B indicates position of panel B. Locality LY-2e. **B)** Uppermost part of prismatic crystal showing constituent nanocrystals. Note development of incomplete, but smooth crystal faces. White letter C indicates position of panel C. Locality LY-2e. **C)** General view of Prismatic Type III crystals (close to the one shown in panel A). White letter D indicates position of panel D. Locality LY-3d. **D)** Enlarged view showing incomplete but complex micro-growth patterns in calcite crystals. Locality LY-3d. **E)** General view of sides of Prismatic Type III crystals. Locality LY-3d. **F)** Same area as in panel E, but rotated 90° to show cross-sectional shapes of the two crystals shown on the right side of panel E. Locality LY-3d.

FIG. 12.– Photomicrographs of Trigonal Prismatic calcite mesocrystals from the distal part of discharge apron at spring LY-2 and the middle part of discharge apron at Stjáni (S). **A)** Cluster of trigonal prisms, each formed of trigonal nanocrystals. White letter B indicates position of panel B. Locality LY-3c. **B, C)** Views along c-axis of trigonal mesocrystal showing perfectly aligned trigonal nanocrystals. Locality LY-3c. **D)** View along c-axis of trigonal mesocrystal formed of aligned trigonal nanocrystals. White letter E indicates position of panel E. Locality S-d. **E)** Enlarged view of corner of trigonal mesocrystal. White letter F indicates position of panel F. **F)** Trigonal nanocrystal with surfaces that appear to be formed of even smaller crystals. Locality S-d.

FIG. 13.– Photomicrographs of incompletely formed dodecahedrons (A–C) from LY-2 and Stjáni (S) and platy-calcite mesocrystals (D–I) from LY-3. **A-C)** General view of unattached dodecahedral calcite crystals characterized by poorly developed crystal faces, edges, and corners. Surfaces, like that in panel C, show that they are formed of nanocrystals. Localities S-d, S-d, and LY-3c, respectively. **D)** Group of platy calcite crystals held in EPS and partly

coated with filamentous microbes. White letters E and F indicate positions of panel E and F, respectively. Locality LY-2d. **E-F)** Enlarged views of platy calcite nanocrystals, all incompletely formed but with a common crystallographic register. Locality LY-2d.

FIG. 14.– Photomicrographs of rhombic Type I calcite mesocrystals from locality LY-2e. **A)** General view of surface of rhombic Type I rhombic mesocrystal formed of numerous nanocrystals. White letter B indicates position of panel B. **B)** Enlarged view showing numerous nanocrystals of variable size and shape in common crystallographic register. White letter C indicates position of panel C. **C)** Enlarged view of rhombic nanocrystals.

FIG. 15.– Photomicrographs of rhombic Type II calcite mesocrystals from locality LY-2c. **A)** Faces and corners of two well developed rhombic mesocrystals. White letter B indicates position of panel B. **B)** Rhombic mesocrystal with smooth, well-defined crystal edges and corner and faces formed of nanocrystals. White letter C indicates position of panel C. **C)** Crystal face showing constituent nanocrystals. **D)** Incompletely developed rhombic mesocrystal with part of one crystal edge being smooth and well formed. White letter E indicates position of panel E. **E)** Smooth crystal edge with neighboring crystal faces displaying constituent nanocrystals. White letter F indicates position of panel F. **F)** Enlarged view of nanocrystals at corner of rhombic crystal. **G)** Rhombic calcite crystals, at various stages of development embedded in opal-A groundmass. White letters H and I indicate positions of panels H and I, respectively. **H)** Incompletely developed crystal with some smooth faces and exposed nanocrystals. **I)** Well-developed rhombic crystal with smooth faces and well-defined crystal edges and corners.

Fig. 16. Photomicrographs of rhombic Type III calcite mesocrystals from Stjáni, locality c. **A)** General view of rhombic Type III crystal. White letters B and C indicates positions of panels

B and C, respectively. **B)** Surface of crystal showing constituent nanocrystals. **C, D)** Oblique views of nanocrystals showing wedge-shaped serrated cross-sectional morphology. Each nanocrystal appears to be formed of slightly overlapping rhombic plates. **E)** Surface of rhombic type III crystal. White letter F indicates position of panel F. **F)** Enlarged views of surface of rhombic crystal showing perfect alignment of constituent nanocrystals.

Fig. 17. Photomicrographs of calcite dendrites from locality LY-2d. **A)** General view of calcite dendrites resting on opal-A substrate and partly covered by filamentous microbes and EPS. White letter B indicates position of panel B. **B–D)** Enlarged view of calcite dendrites with each dendrite being formed of three main branches and locally, smaller secondary branches.

Table 1. Water analyses for Lýsuhóll (see Fig. 2A for location of samples). All values given in mg l^{-1}. Samples from Lysuholl[1], Lysuholl[2], and Lysuholl[3] are probably from spring LY-1, which Pentecost referred to as Stjáni. Saturation indices were calculated using SOLMINEQ88 (Kharaka et al., 1988). Field pH values were used in calculations.

Locality	T°C	pH	Na	K	Ca	Mg	HCO_3	SO_4	Cl	SiO_2	Fe	B	Mn	Sr	Calcite saturation	Silica (am) saturation
LY-1	46.1	6.62	434	37	42.0	26.0	1350	39.0	70.0	165	0.53	0.5	0.2	0.4	-0.005	-0.012
LY-2	20.2	6.31	359	31	62.0	16.0	1100	41.0	60.0	146	0.23	0.4	0.5	0.34	-0.527	0.124
LY-3	37.3	6.15	373	33	37.0	17.0	1130	41.0	60.0	148	0.22	0.4	0.46	0.35	-1.059	0.004
LY-4	10.1	7.28	2.1	0.5	15.0	2.1	56	3.4	13.0	6.6	0.03	0.0	0.01	0.03	-1.37	-1.149
LY-5	15.6	8.67	13	24	22.0	13.0	737	42.0	58.0	17.8	0.28	0.3	0.11	0.19	1.11	-0.78
Lysuholl[1]	57.0	6.72	434	33.9	93.4	17.8		43.0	80.0	219						
Lysuholl[2]	60.0	6.88	486	36.5	79.9	20.8		43.1	69.5	178						
Lysuholl[3]	41.6	6.4	406	29.0	136.0	32.0	1520	38.0	84.0	171	2.6	0.57	0.05	0.0		
Lysuholl[4]	30.0	6.4	467	25.7	148.0	43.8		50.3	88.6	143	3.1	0.53				

Locations:

LY1–LY-5: This study.
Lysuholl[1]: Analysis from Fridleifsson and Ármannsson (1999)
Lysuholl[2]: Analysis from Arnórsson and Barnes (1983)
Lysuholl[3]: Analysis from White et al. (1963, their Table 25)
Lysuholl[4]: Analysis from Kjartansdóttir (2014, her Table 6)


A
24°W
21°W
18°W
15°W
Arctic Circle
66°N
65°N
Snaefellsnes
Lýsuhóll
Reykjavik
Vatnajökull
100 km
North Atlantic Ocean
B
700
Hrafntinnuborg
600
500
100
N
LY-2
LY-3
Hrútsgill
Stjani
Lýsuhóll
Vatnsholtavon
400
300
200
75
25
25
Lýsuvatn
Torfavatn
1 km
North Atlantic Ocean

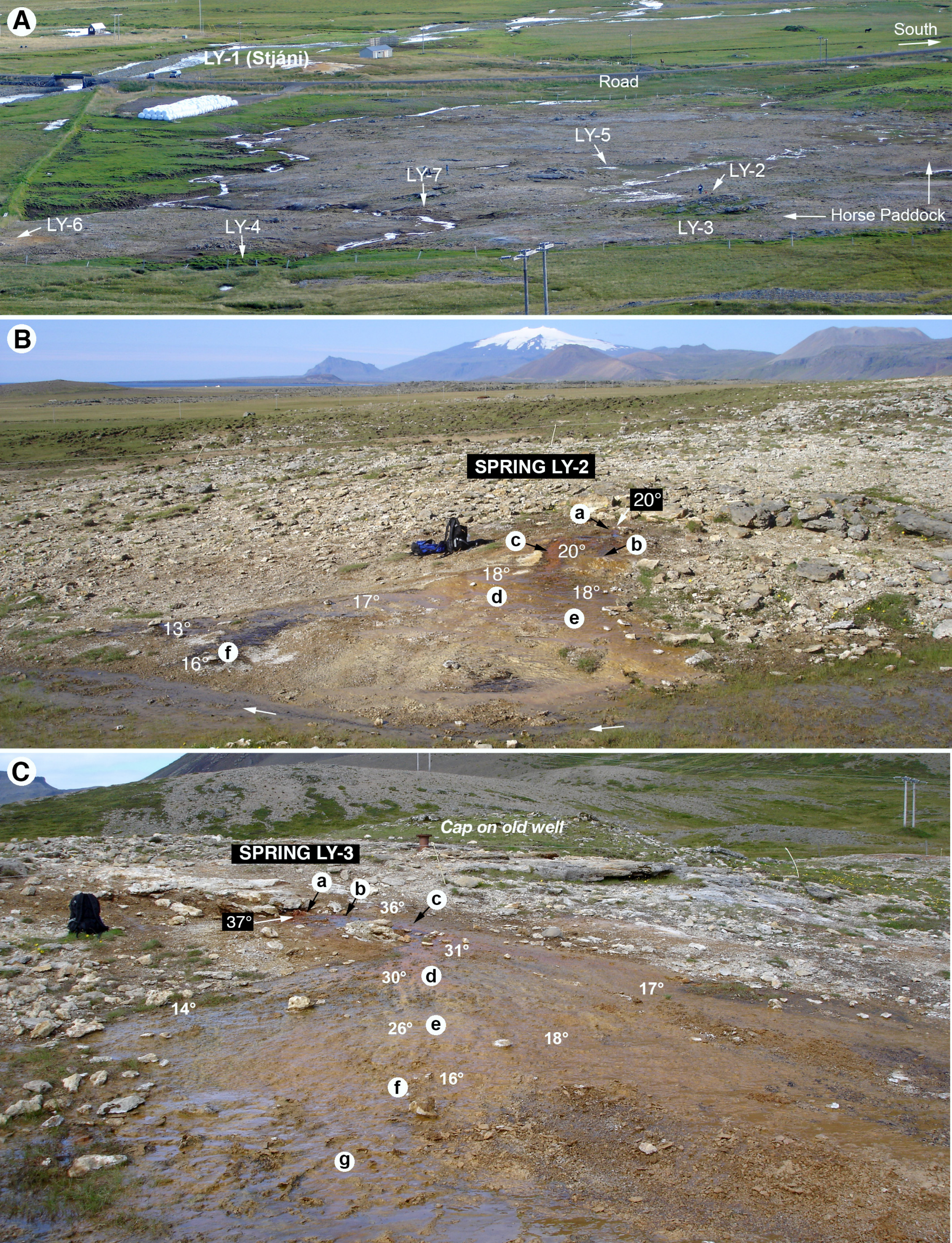
A
LY-1 (Stjáni)
South
Road
LY-5
LY-7
LY-2
LY-6
LY-4
LY-3
Horse Paddock
B
SPRING LY-2
20°
a
c
20°
b
18°
d
18°
17°
e
13°
f
16°
C
Cap on old well
SPRING LY-3
a
b
c
36°
37°
31°
d
30°
17°
14°
e
26°
18°
f
16°
g

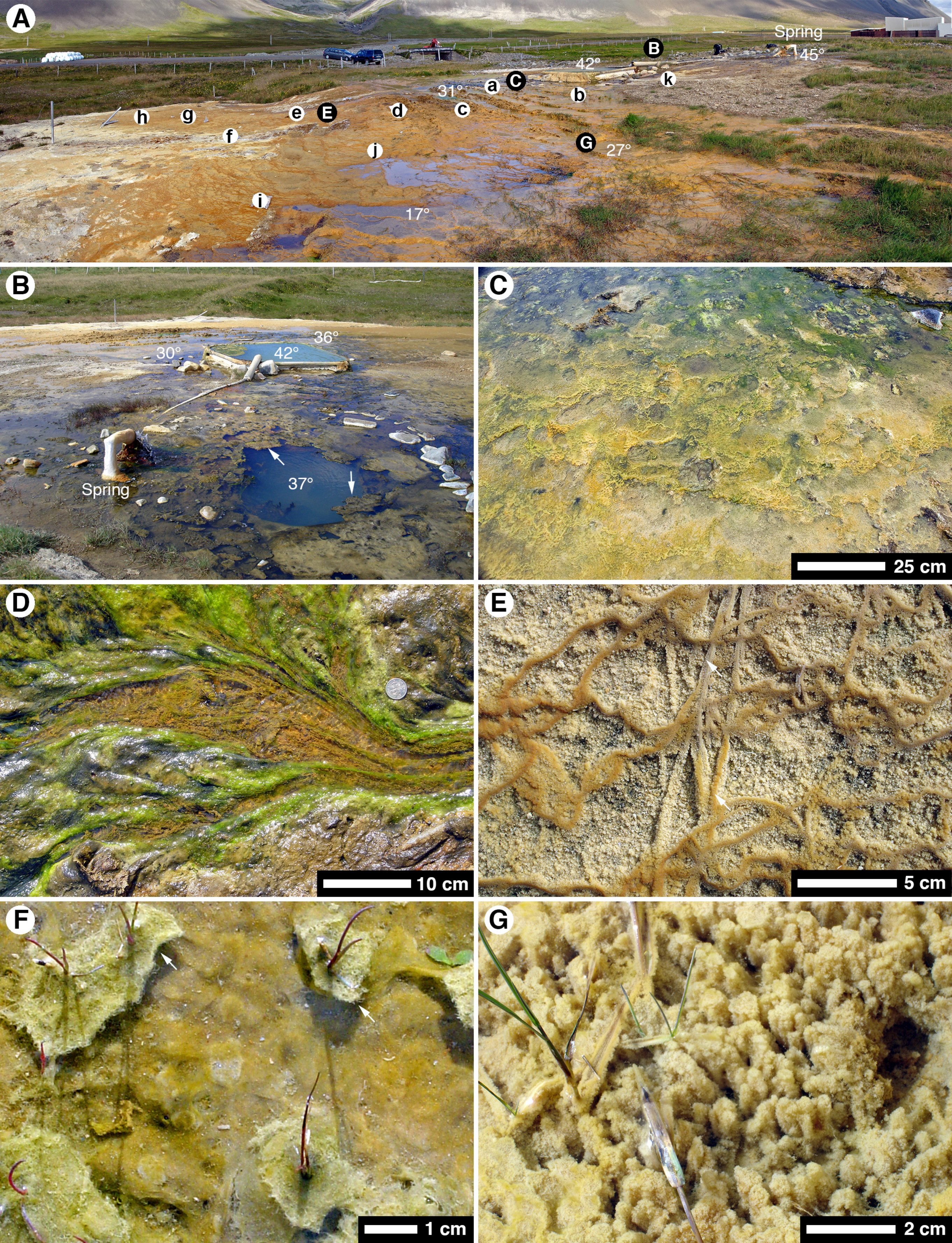
A
Spring
45°
B
42°
a
C
k
31°
b
c
h
g
e
E
d
f
j
G
27°
i
17°
B
36°
30°
42°
Spring
37°
C
25 cm
D
10 cm
E
5 cm
F
1 cm
G
2 cm

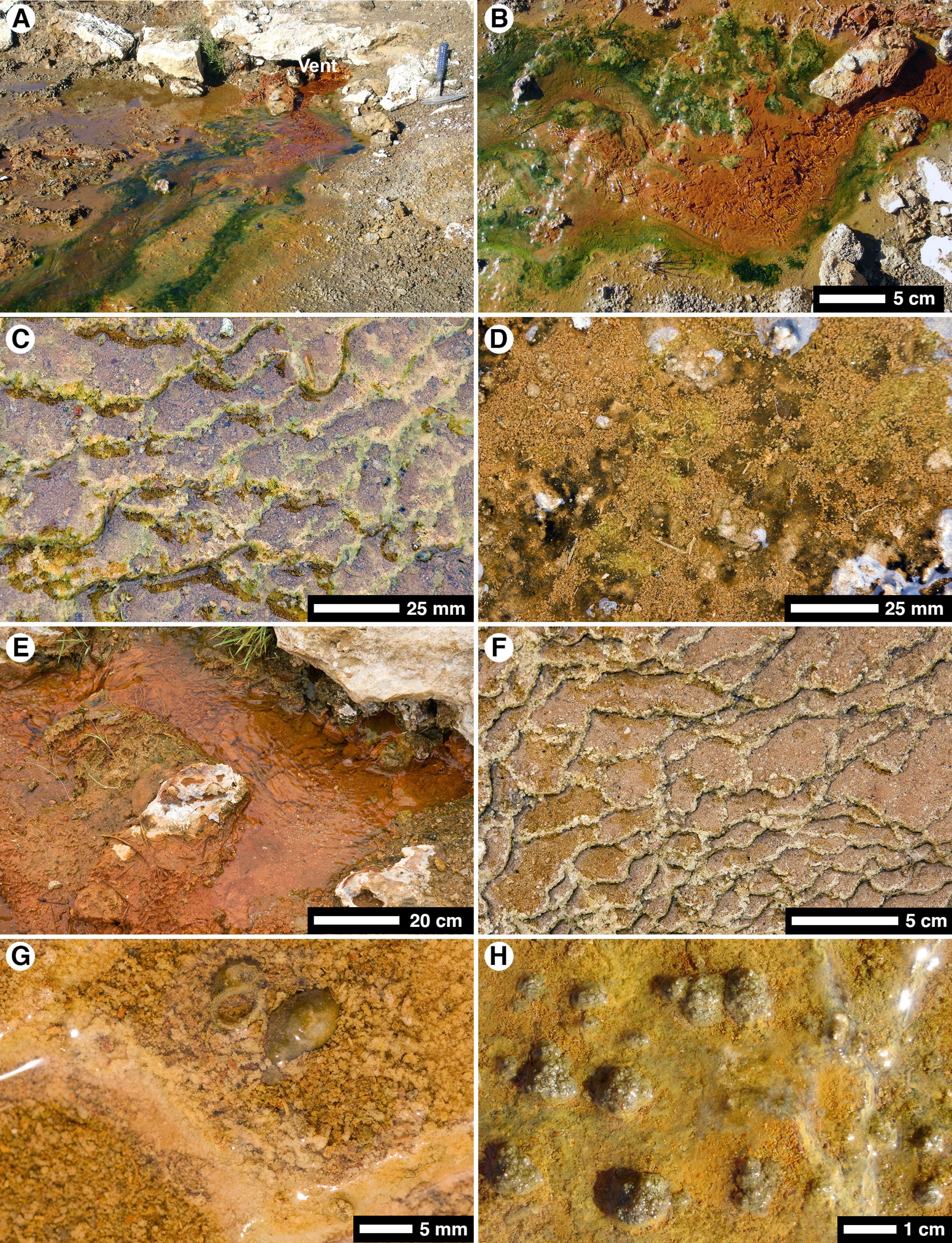
A
Vent
B
5 cm
C
25 mm
D
25 mm
E
20 cm
F
5 cm
G
5 mm
H
1 cm

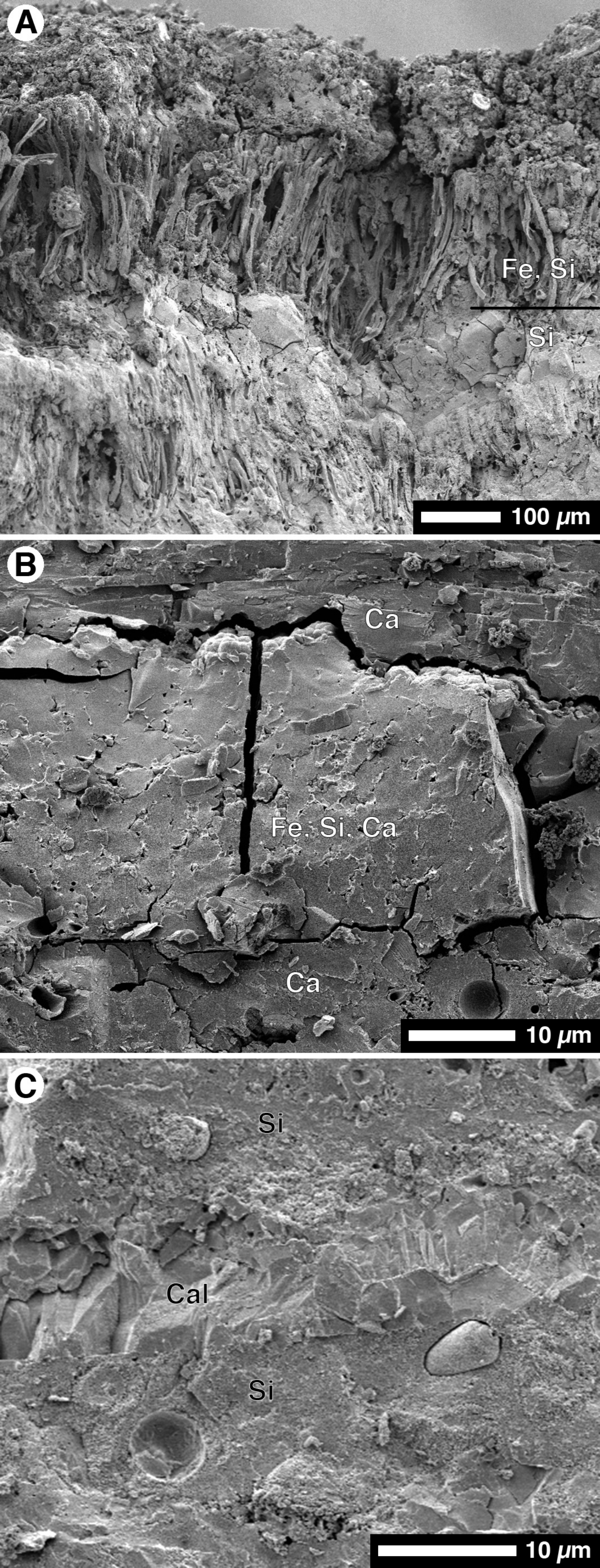
A
Fe, Si
Si
100 μm
B
Ca
Fe, Si, Ca
Ca
10 μm
C
Si
Cal
Si
10 μm

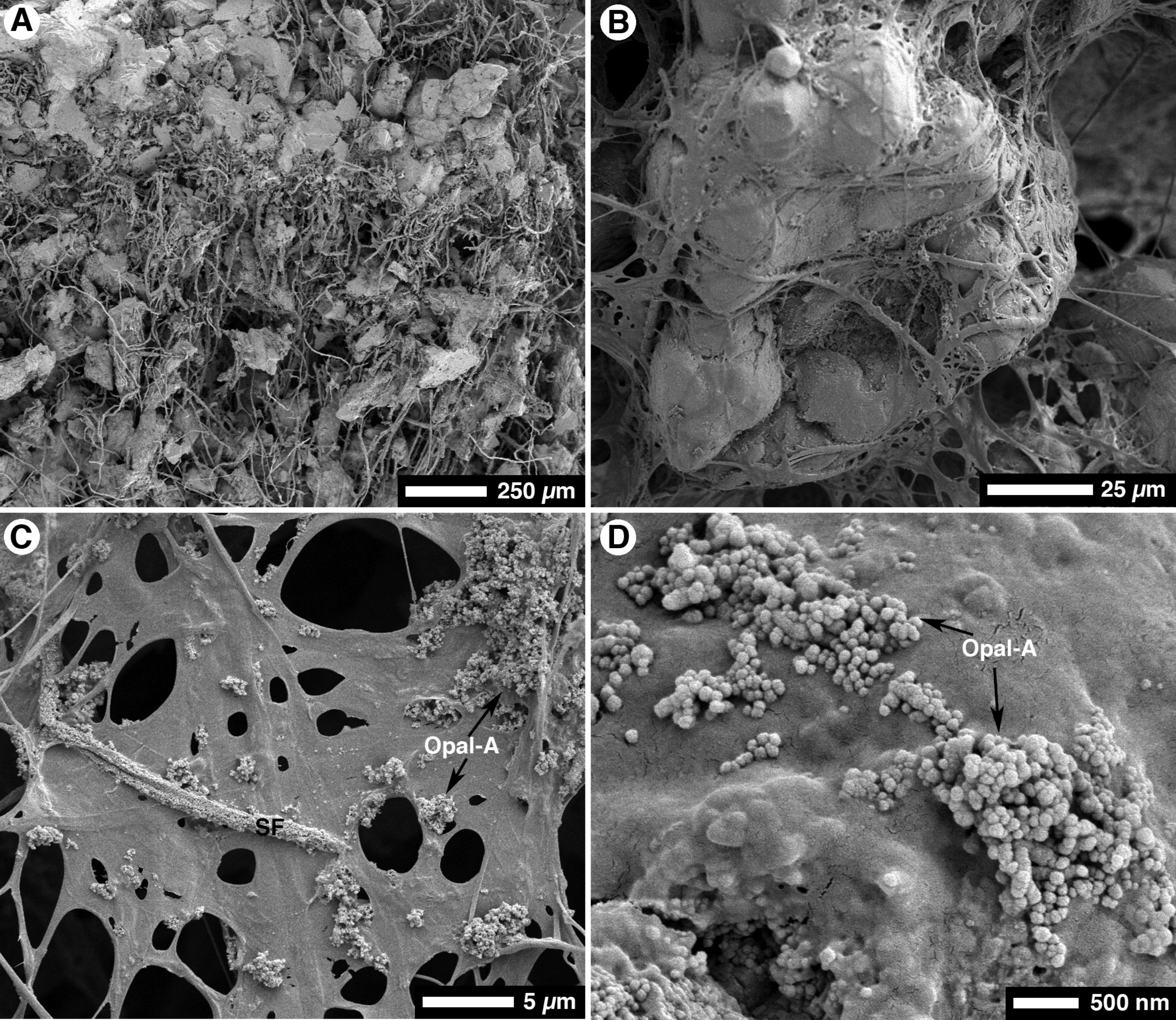
A
250 µm
B
25 µm
C
Opal-A
SF
5 µm
D
Opal-A
500 nm

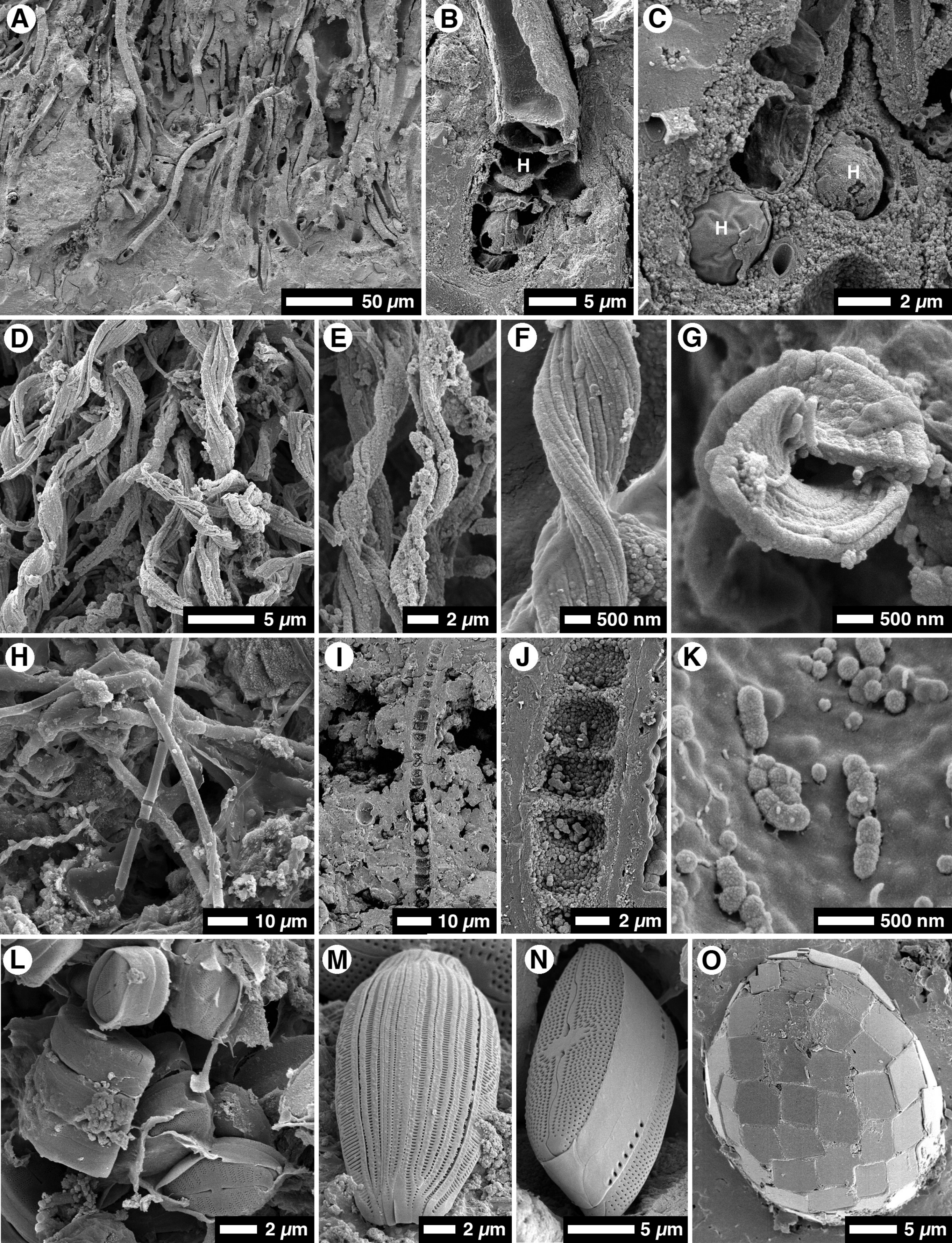
A
50 μm
B
H
5 μm
C
H
H
2 μm
D
5 μm
E
2 μm
F
500 nm
G
500 nm
H
10 μm
I
10 μm
J
2 μm
K
500 nm
L
2 μm
M
2 μm
N
5 μm
O
5 μm

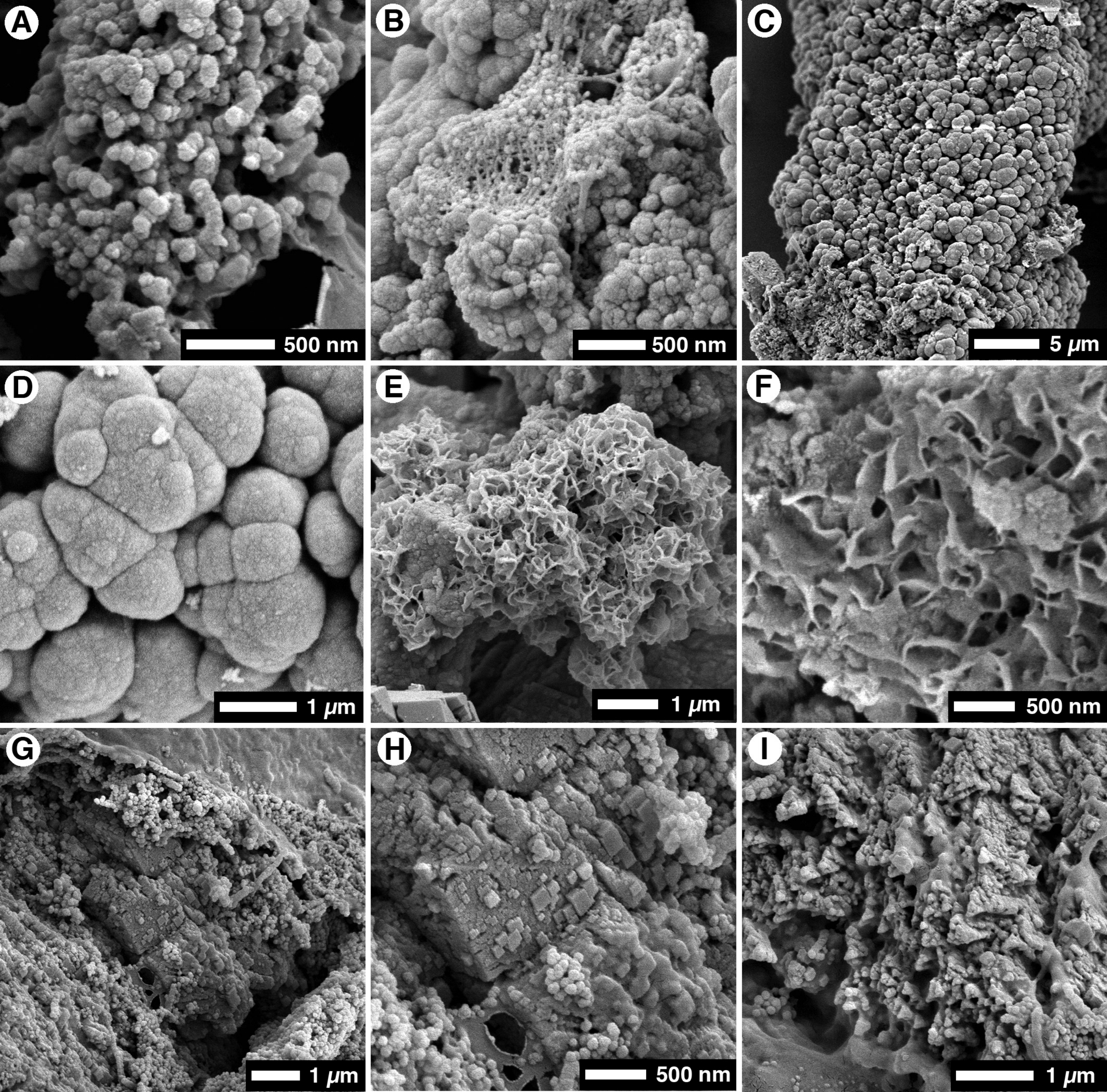
A
500 nm
B
500 nm
C
5 μm
D
1 μm
E
1 μm
F
500 nm
G
1 μm
H
500 nm
I
1 μm

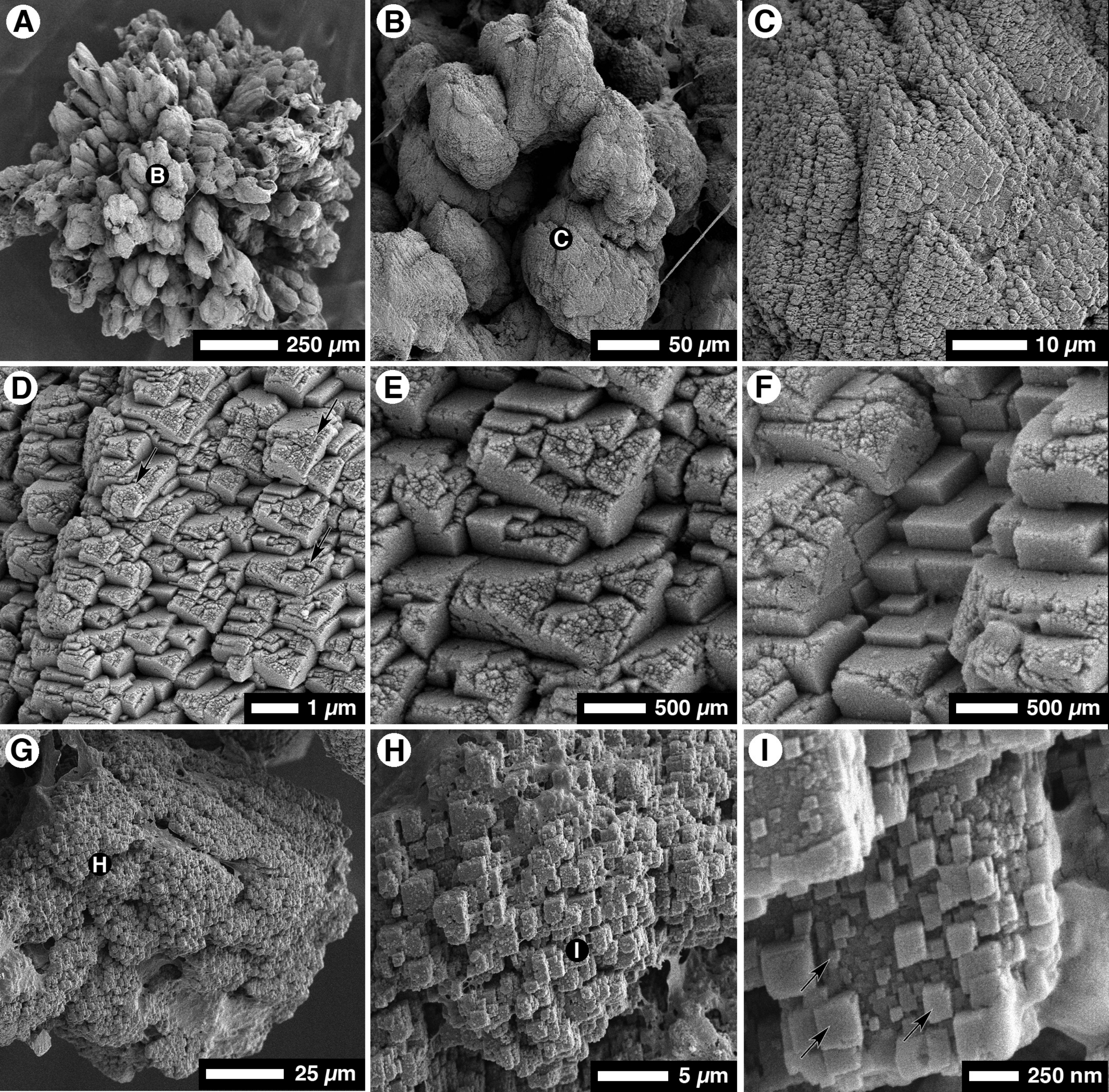
A
B
250 μm
B
C
50 μm
C
10 μm
D
1 μm
E
500 μm
F
500 μm
G
H
25 μm
H
I
5 μm
I
250 nm

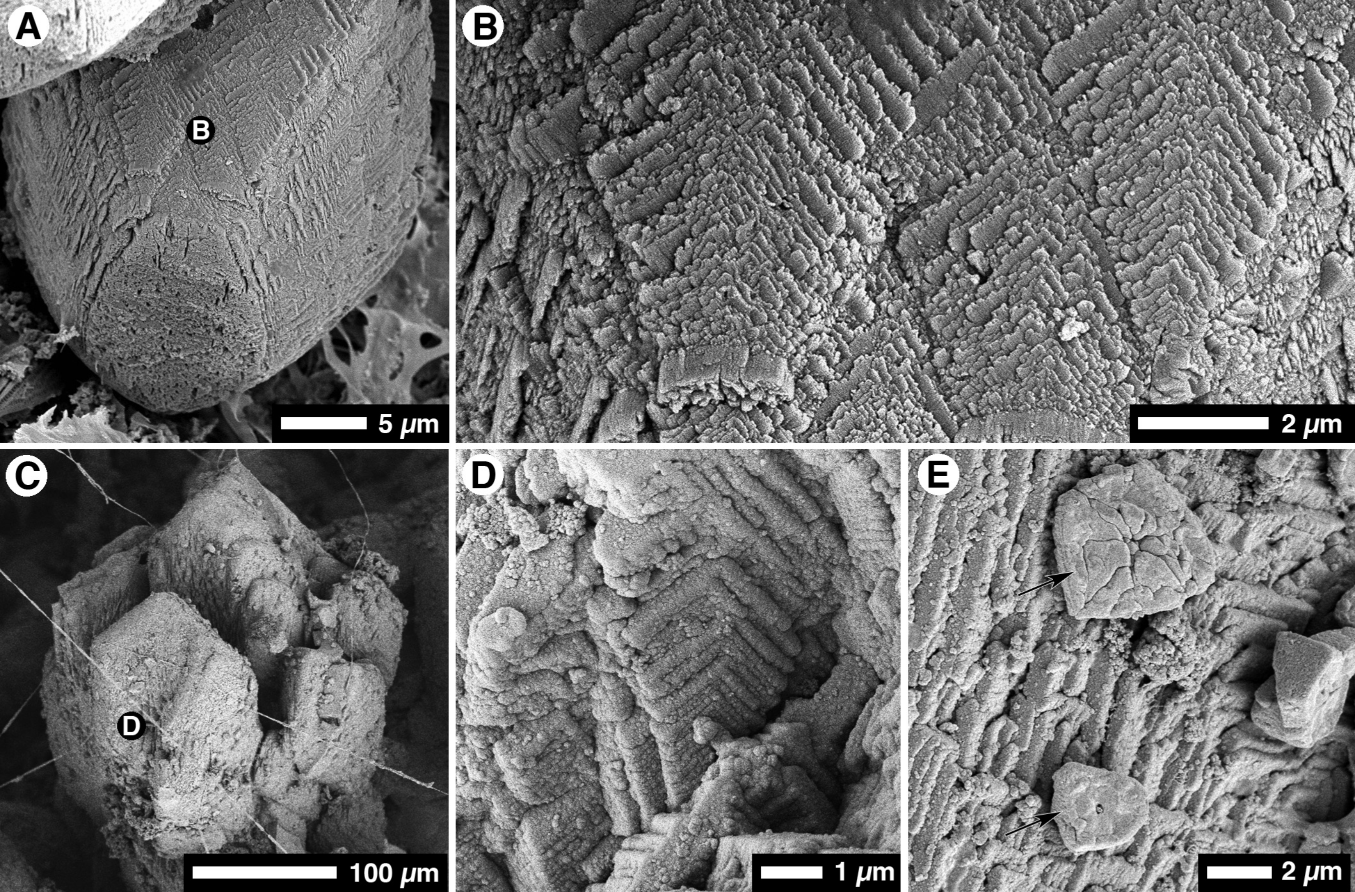
A
B
5 μm
B
2 μm
C
D
100 μm
D
1 μm
E
2 μm

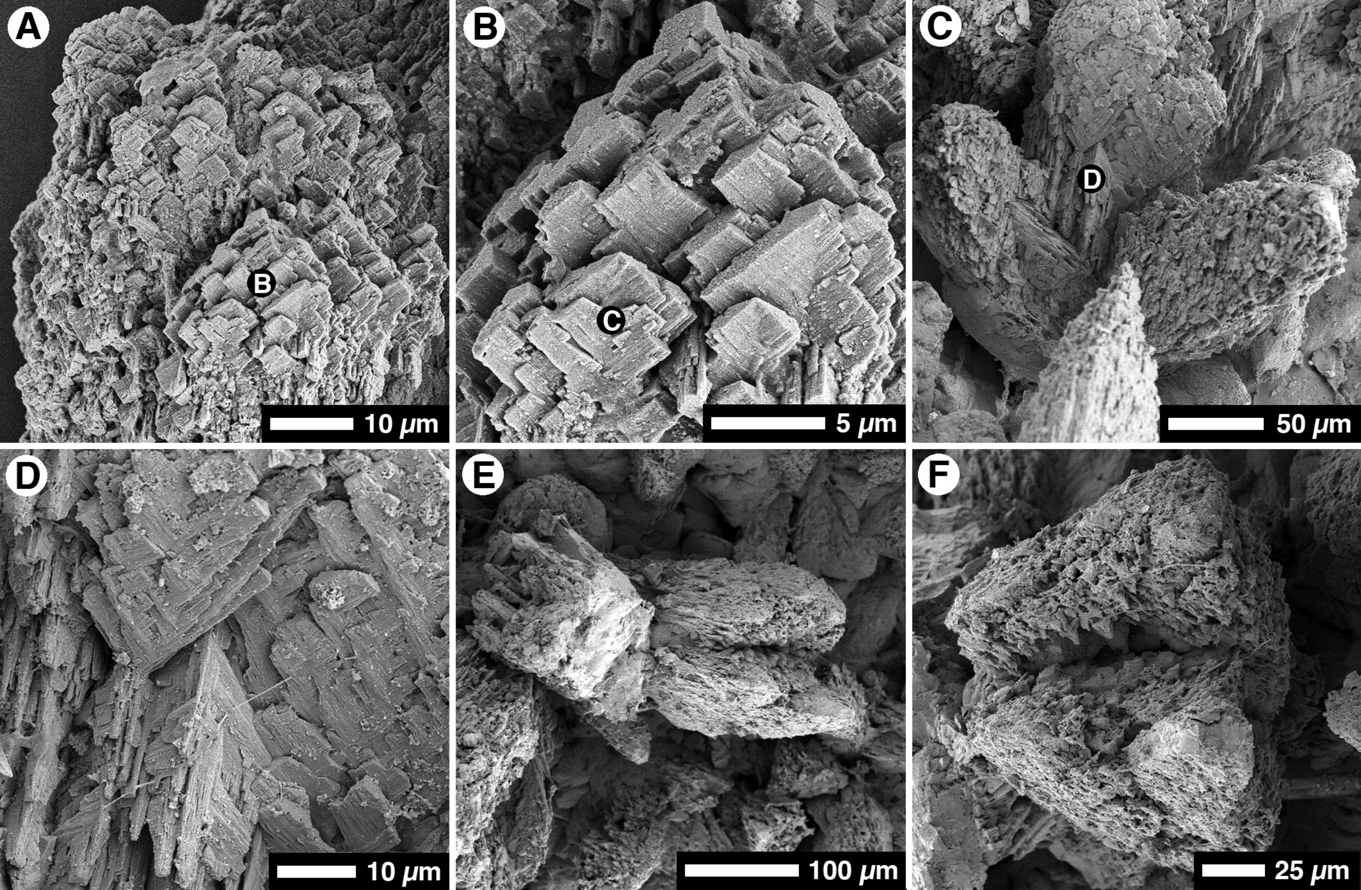
A
B
10 μm
B
C
5 μm
C
D
50 μm
D
10 μm
E
100 μm
F
25 μm

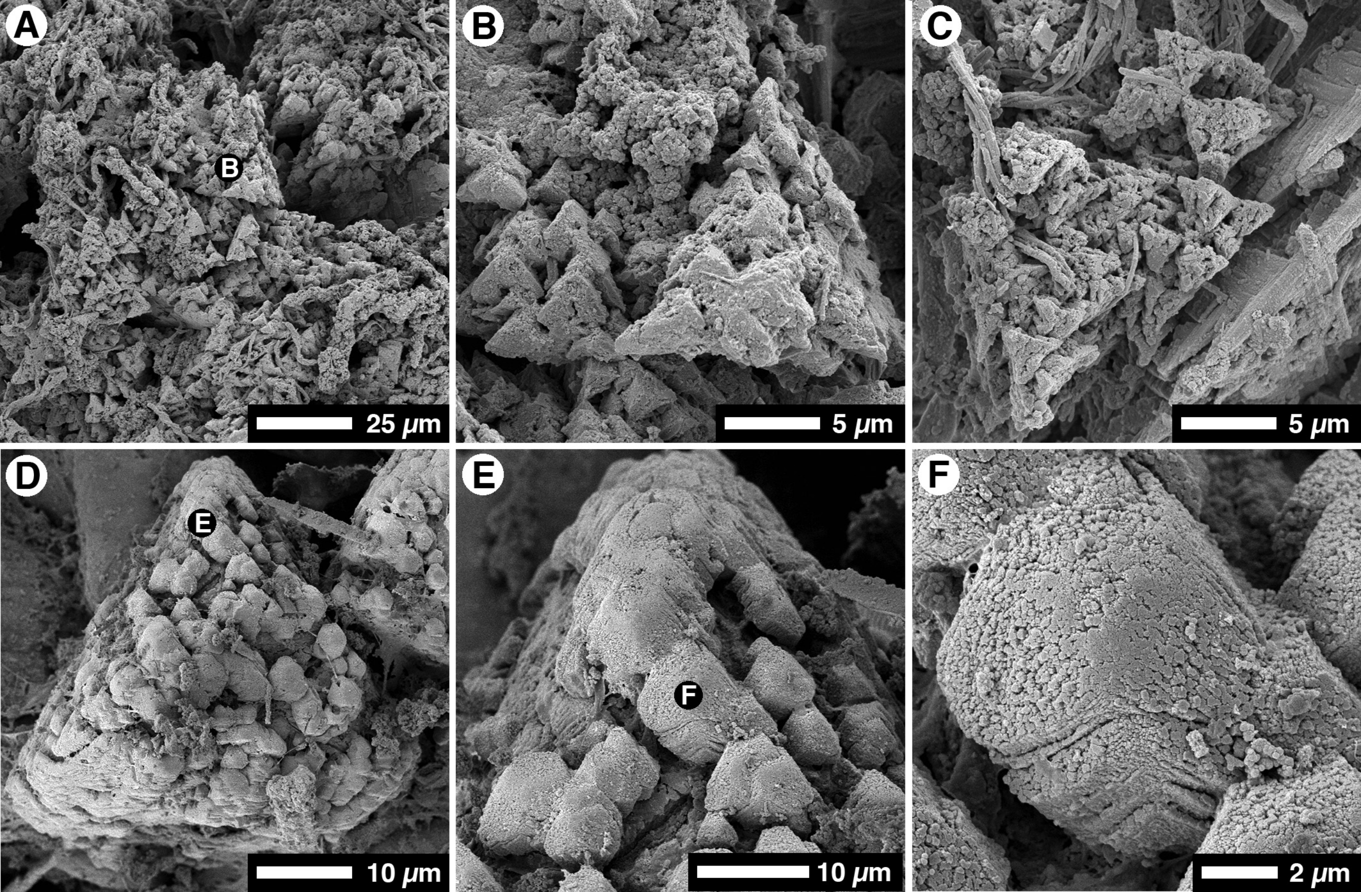
A
B
25 μm
B
5 μm
C
5 μm
D
E
10 μm
E
F
10 μm
F
2 μm

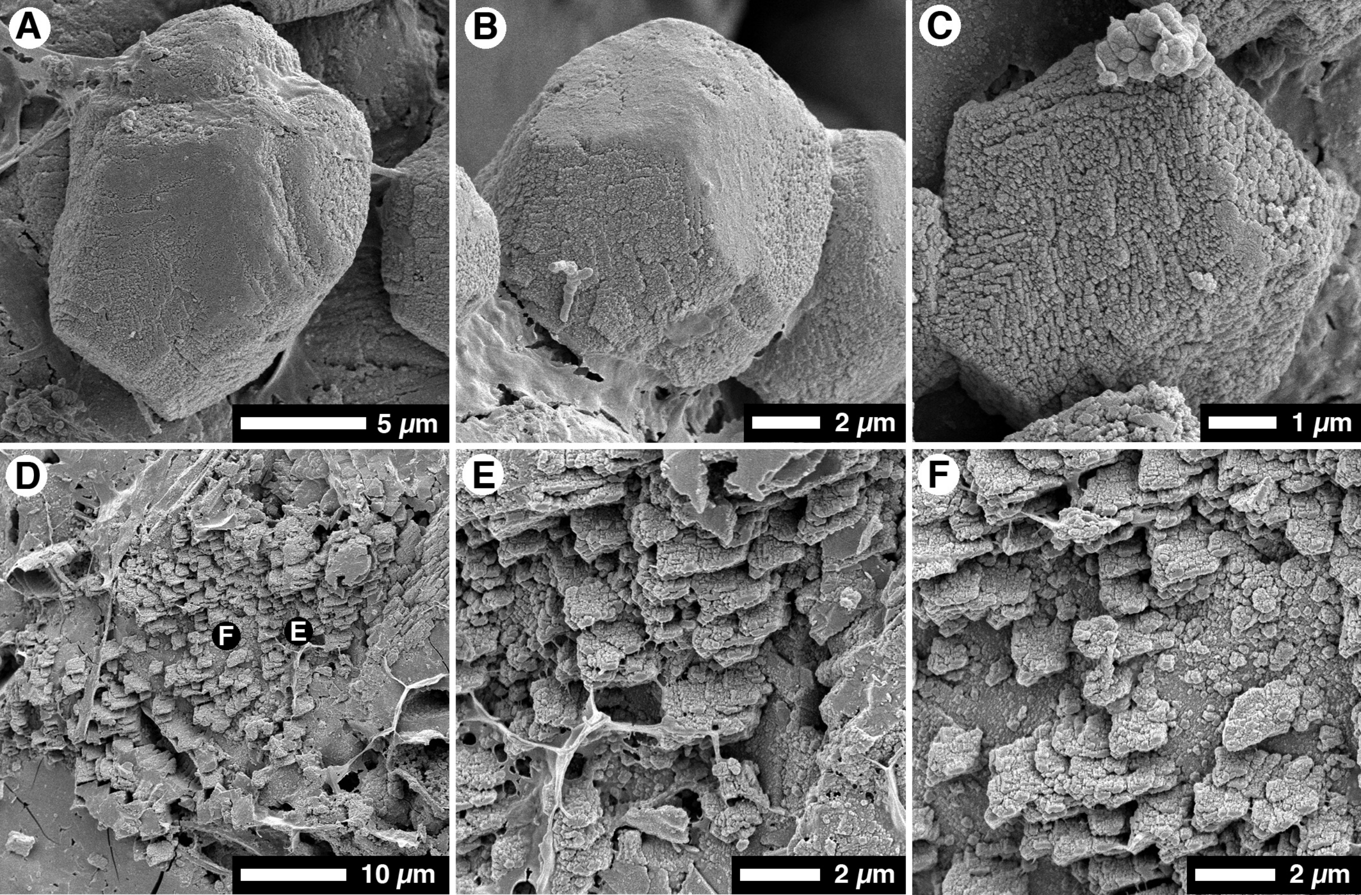
A
5 μm
B
2 μm
C
1 μm
D
F
E
10 μm
E
2 μm
F
2 μm

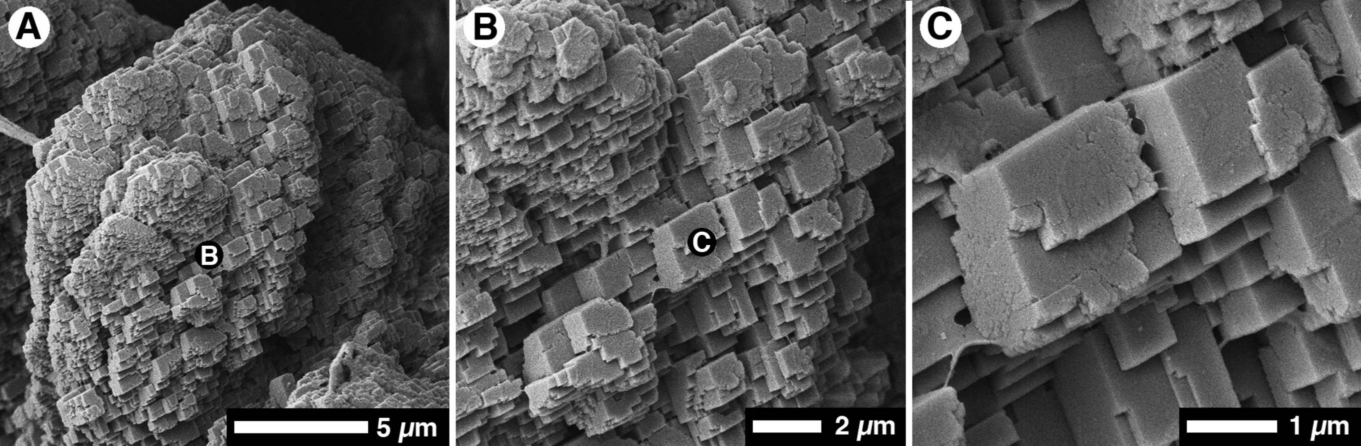
A
B
5 μm
B
C
2 μm
C
1 μm

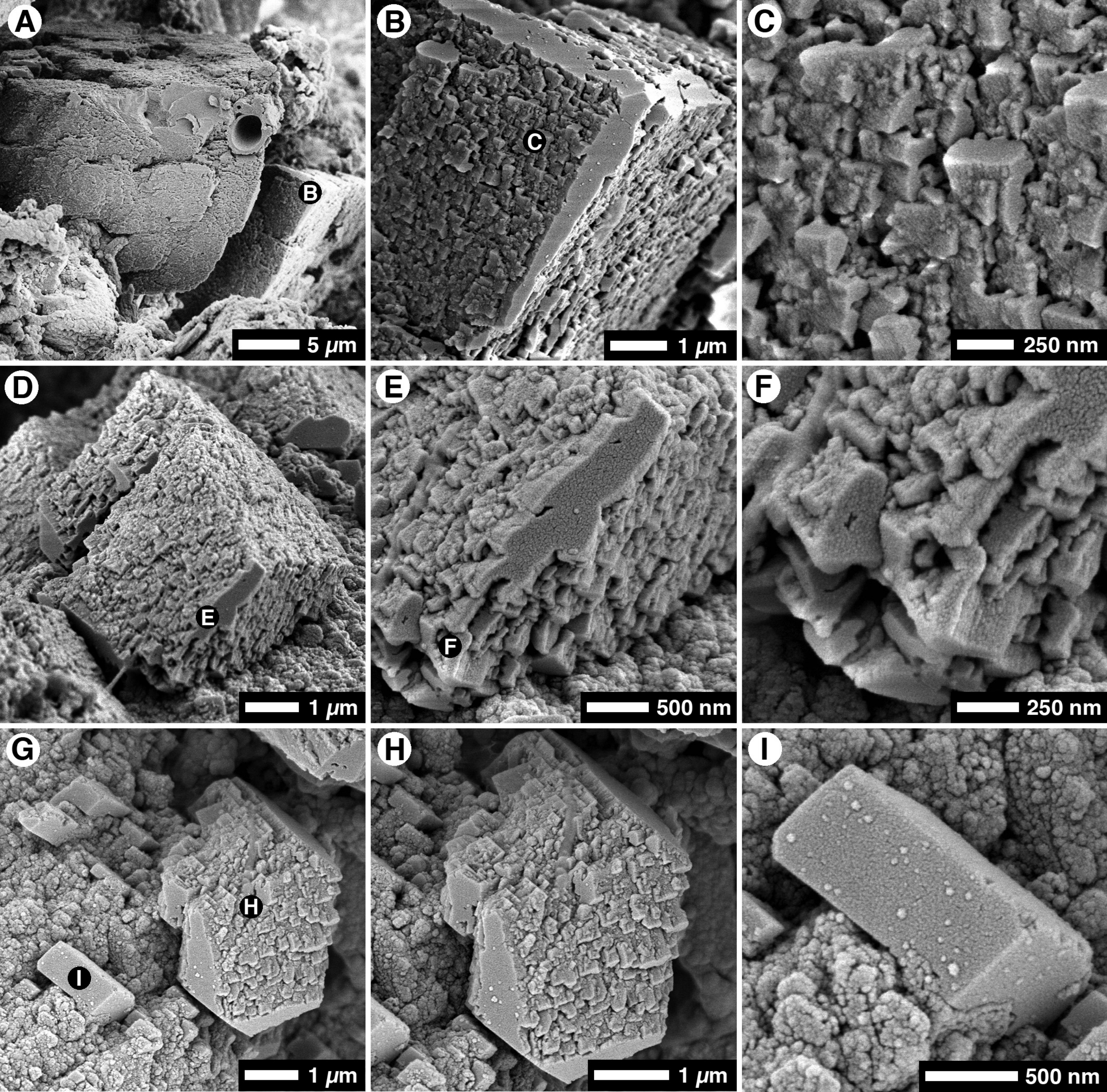
A
B
5 μm
B
C
1 μm
C
250 nm
D
E
1 μm
E
F
500 nm
F
250 nm
G
H
I
1 μm
H
1 μm
I
500 nm

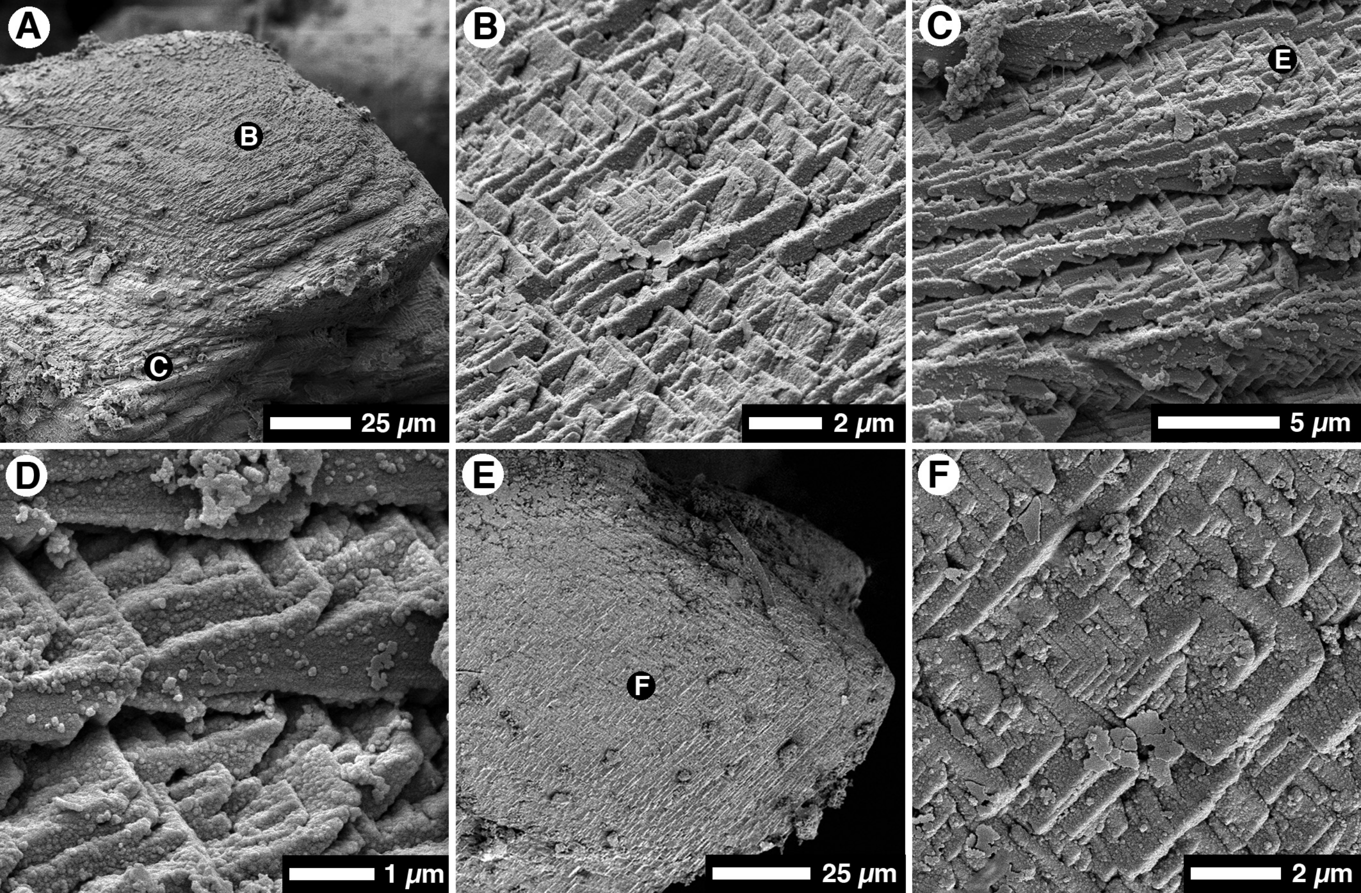
A
B
C
25 μm
B
2 μm
C
E
5 μm
D
1 μm
E
F
25 μm
F
2 μm

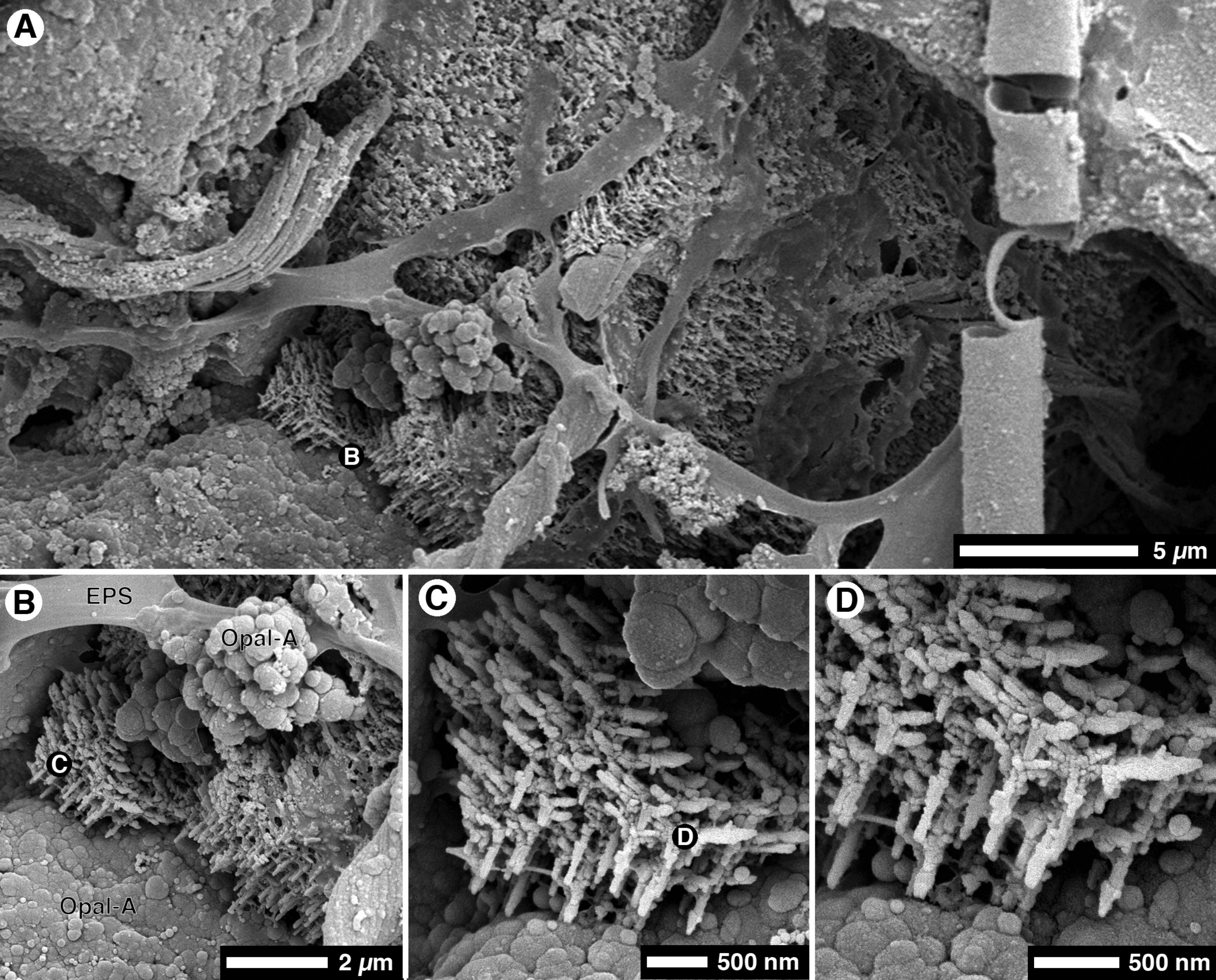
A
B
5 μm
B
EPS
Opal-A
C
Opal-A
2 μm
C
D
500 nm
D
500 nm